

evaporator until the volume of the sample was about 50  $\mu$ l.

**Capillary HPLC Separation and Sequencing**—After evaporation, 10  $\mu$ l of the sample was injected into an ABI 173 A MicroBlotter Capillary HPLC System (PerkinElmer Life Sciences) (45). The sample was manipulated according to the manufacturer's instructions (User's Manual, PerkinElmer Life Sciences). Meanwhile, the blotted membrane from the capillary HPLC separation using a  $C_{18}$  column (5  $\mu$ m, 1.5  $\times$  150 mm, PerkinElmer) was in contact with an imaging plate for 48 h prior to autoradiography analysis. The PVDF membrane was aligned with the chromatogram of a peptide map from the ABI 173 A MicroBlotter Capillary HPLC System. Portions of the PVDF membrane were excised for sequencing on an Applied Biosystems Procise Sequencer with reference to the autoradiogram.

**Docking of UCN-01 to hAGP**—The structure of hAGP has not previously been experimentally determined. As a model of the three-dimensional structure of hAGP for ligand docking, we used the modeled structure of hAGP obtained by Kopecky *et al.* (46). The initial structure of UCN-01 was taken from the crystal structure of the Chk1-UCN-01 complex (47, PDB ID 1NVQ). The docking calculation of UCN-01 to hAGP was performed using the SYBYL FlexX (48) under the condition that UCN-01 interacts with Trp-160. During the docking calculation, the structure of hAGP and the ring conformation of UCN-01 were kept rigid. The docking algorithm produced 158 different placements of UCN-01 in hAGP. All placements were evaluated by SYBYL CScore and were then ranked using AASS (Average of Auto-Scaled Scores), as follows in Equation 1.

$$\text{AASS}^{\text{placement}} = \frac{\sum_i \frac{i_{\text{Score}}^{\text{placement}} - \text{mini}_{\text{Score}}}{\text{max}(i_{\text{Score}}) - \text{min}(i_{\text{Score}})}}{n} \quad (\text{Eq. 1})$$

In the AASS calculation,  $n = 5$  and  $i = \text{F\_Score}$  (48),  $\text{G\_Score}$  (49),  $\text{PMF\_Score}$  (50),  $\text{D\_Score}$  (51),  $\text{ChemScore}$  (52). Although the top 5 placements had nearly the same AASS values, they were classified into two types of binding modes. For each type, we chose the placement with the best AASS value as the candidate binding mode. In the type I model, UCN-01 is bound to a hydrophobic pocket formed by Val-41, Ile-44, Phe-48, and Val-156. In the type II model, UCN-01 is packed into a hydrophobic pocket consisting of Ile-28, Pro-131, Leu-138, Tyr-157, and Trp-160.

**Refinement of Docking Models**—To refine the docking models, the coordinates of the atoms of UCN-01 and the atoms of hAGP within 10 Å from UCN-01 were optimized to reduce the root mean square of the gradients of potential energy below 0.05 kcal mol<sup>-1</sup> Å<sup>-1</sup> using SYBYL 6.9.1 (Tripos, Inc., 2003). The Tripos force field was used for the molecular energy calculation. The AMBER 7 charges (53) were used as the atomic charges for hAGP. The Gasteiger-Hückel charges (54–57) were used as the charges for UCN-01. The cut-off distance for the non-bonded interactions was 10 Å. The distance-dependent dielectric constant of  $4r$  was used. Due to the lack of hydrogen atoms in the modeled structure of hAGP, the initial positions of the hydrogen atoms in the hAGP were generated by the SYBYL.

**Statistical Analysis**—Statistical analysis of differences was performed by one-way ANOVA followed by the modified Fisher's least squares difference method.

## RESULTS

**Photolabeling of [<sup>3</sup>H]UCN-01 to hAGP**—The autoradiogram in Fig. 2 shows that the band of radiolabeled protein appeared only upon the photoirradiation of hAGP with [<sup>3</sup>H]UCN-01. The radioactivity band indicated the incorporation of [<sup>3</sup>H]UCN-01 to hAGP via photoirradiation. No band of radiolabeled protein could be observed for the sample without irradiation indicating that no covalent attachment of [<sup>3</sup>H]UCN-01 to hAGP occurred in the dark. Exposure to light for 30 min was sufficient for the photoincorporation of [<sup>3</sup>H]UCN-01 to hAGP (Fig. 3). The results indicate that [<sup>3</sup>H]UCN-01 is photoactivatable and stable in the dark.

**Competition Experiments**—In a previous study using ultracentrifugation methods, it was concluded that the binding site for UCN-01 on hAGP partly overlaps with the binding site for basic drugs, acidic drugs, and steroid hormones (58). In the present photolabeling experiment, in order to determine the photolabeling specificity of [<sup>3</sup>H]UCN-01, we used staurosporine and UCN-02 (a stereoisomer of UCN-01), which also bind

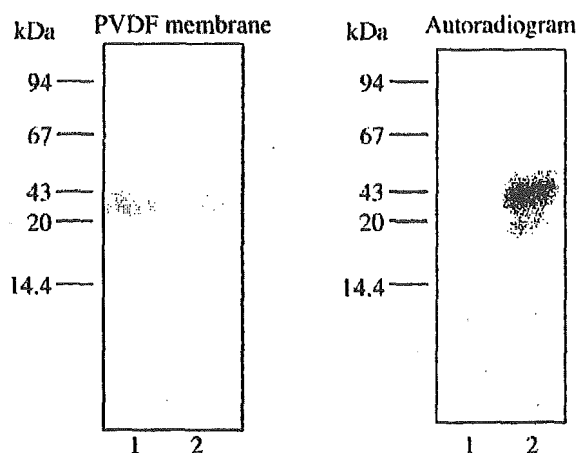


Fig. 2. Photolabeling of hAGP with [<sup>3</sup>H]UCN-01. Lane 1, sample taken just prior to photoirradiation. Lane 2, sample taken after 30-min photoirradiation (>300 nm). 50  $\mu$ M hAGP was incubated with 0.08  $\mu$ M [<sup>3</sup>H]UCN-01 for 60 min prior to photoirradiation. The samples were separated with 10% SDS-PAGE and electroblotted onto a PVDF membrane for autoradiographic analysis.

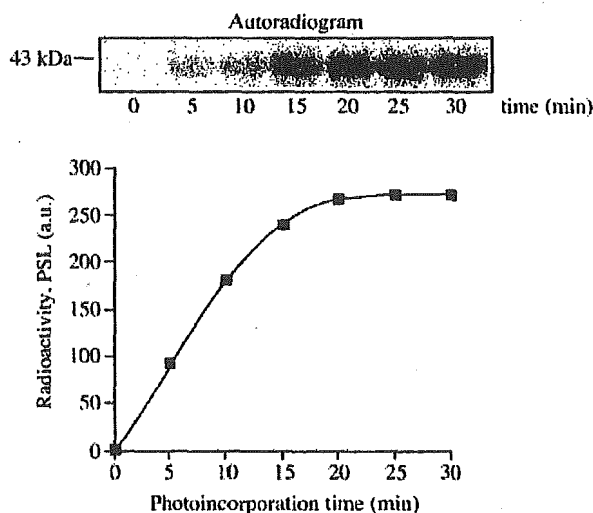


Fig. 3. Time course of [<sup>3</sup>H]UCN-01 photoincorporation. 50  $\mu$ M hAGP was incubated with 0.08  $\mu$ M [<sup>3</sup>H]UCN-01 for 60 min prior to photoirradiation. Aliquots of 100  $\mu$ l were taken from the mixture solution at each time point as stated in the figure during irradiation until 30 min. All samples were separated with 10% SDS-PAGE and electroblotted onto a PVDF membrane for autoradiographic analysis. PSL, photostimulated luminescence.

hAGP, as competitors. All staurosporine analogs significantly inhibited photoincorporation, by more than 60% (Fig. 4). Other competitors that we used were representatives of other hAGP ligands: an acidic drug (warfarin), a basic drug (propranolol), and a steroid (progesterone). Warfarin and propranolol inhibited binding by less than 30%, but to a significant degree, whereas progesterone inhibited binding by about 60% (Table I).

**Amino Acid Sequence of the Photolabeled Tryptic Peptides**—Tryptic peptides of the hAGP photolabeled with [<sup>3</sup>H]UCN-01 were separated by reverse phase HPLC using a  $C_{18}$  column. The major radioactive peptides were eluted in 10.5–11.5 min (Fig. 5, A and B). The fractions eluted within this time frame were collected and concentrated with a SpeedVac evaporator for further capillary HPLC analysis. The concentrated sample from previous HPLC analysis was separated and simulta-

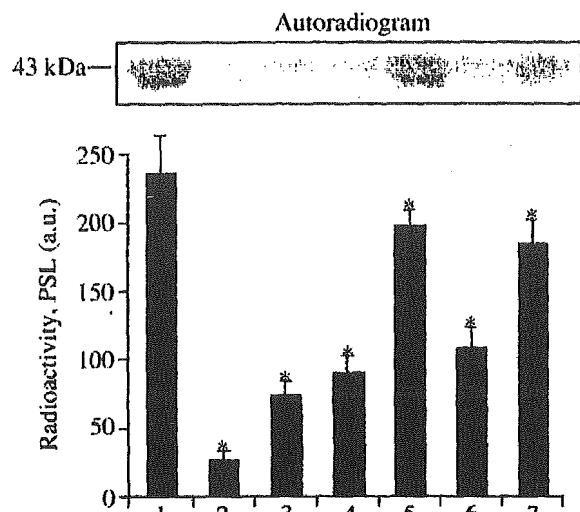


FIG. 4. Photolabeling of hAGP with [ $^3$ H]UCN-01 in the presence of competitors. Lane 1, no competitor; lane 2, cold UCN-01; lane 3, staurosporine; lane 4, UCN-02; lane 5, warfarin; lane 6, progesterone; lane 7, propranolol. 50  $\mu$ M hAGP was incubated with 0.08  $\mu$ M [ $^3$ H]UCN-01 and 250  $\mu$ M competitors for 60 min prior to photoirradiation. The incubation mixture was irradiated for 30 min, separated with 10% SDS-PAGE, and electroblotted onto a PVDF membrane for autoradiographic analysis. \*, statistically significant, compared with no competitor;  $p < 0.01$ . PSL, photostimulated luminescence.

TABLE I  
Binding affinity constant and inhibition percentage by the competitors

Competitor	$K_a$ $M^{-1}$	Inhibition %
Cold UCN-01 <sup>a</sup>	$2.88 \times 10^6$	86.38
Staurosporine <sup>a</sup>	$1.13 \times 10^7$	68.54
UCN-02 <sup>a</sup>	$1.48 \times 10^6$	61.52
Warfarin <sup>b</sup>	$1.08 \times 10^6$	16.43
Progesterone <sup>b</sup>	$1.00 \times 10^6$	58.71
Propranolol <sup>b</sup>	$2.98 \times 10^5$	26.26

<sup>a</sup> Binding constant data taken from Ref. 38.

<sup>b</sup> Binding constant data taken from Ref 59.

neously blotted onto a strip of PVDF membrane using an ABI 173 A MicroBlotter Capillary HPLC System. Autoradiographic analysis of the PVDF membrane indicated that the radioactive spot corresponded to the peak observed at 84–85 min (Fig. 6, A and B). Edman sequencing of this spot revealed an amino acid sequence of SDVVYTDKX (Fig. 7), corresponding to Ser-153 to Lys-161 of hAGP.

**Photolabeling of Wild-type and Mutant rhAGP with [ $^3$ H]UCN-01**—Mutation of the 160th Trp residue of rhAGP to an Ala residue (W160A) caused a significant decrease in photoincorporation, by about 80%. In contrast, there was no significant difference in photoincorporation of [ $^3$ H]UCN-01 between wild-type rhAGP and the rhAGP mutants W25A and W122A (Fig. 8).

**Docking of UCN-01 to hAGP**—We constructed models of the docking of UCN-01 into the binding cavity of hAGP around Trp-160, using the three-dimensional molecular model of hAGP published by Kopecky *et al.* (46), to map the possible binding sites of hAGP. Molecular modeling calculations revealed 2 potential binding sites, type I and type II, around Trp-160, both of which were located in the outer region of hAGP (Fig. 9A). Table II shows the distance and nature of interaction between donors and acceptors in the models of types I and II. In the type II model, UCN-01 is packed into a surface cleft consisting of Ile-28, Pro-131, Glu-132, Lys-135, Leu-138, Tyr-157, Trp-160,

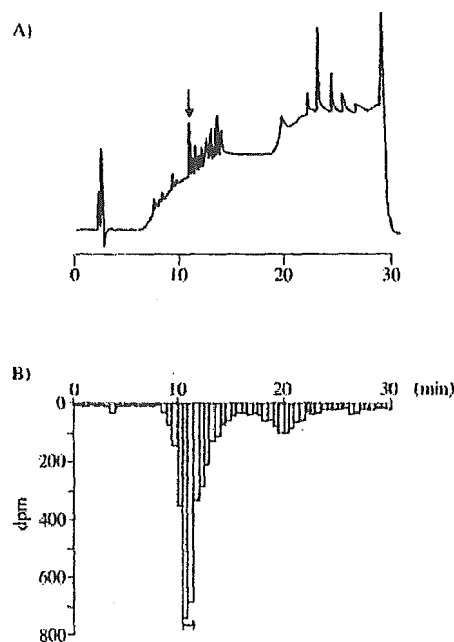


FIG. 5. Reverse-phase HPLC separation of tryptic peptides of hAGP photolabeled with [ $^3$ H]UCN-01. A, chromatogram of tryptic peptides of hAGP photolabeled with [ $^3$ H]UCN-01 detected at UV absorption wavelength of 210 nm. B, radioactivity of the reverse-phase fractions (200  $\mu$ l) was determined by scintillation counting. An aliquot of 20  $\mu$ l of the tryptic peptides was applied to a  $C_{18}$ -column and eluted at 1 ml/min using an aqueous acetonitrile gradient in the presence of 0.1% trifluoroacetic acid (from 5 to 95% acetonitrile over the course of 40 min).

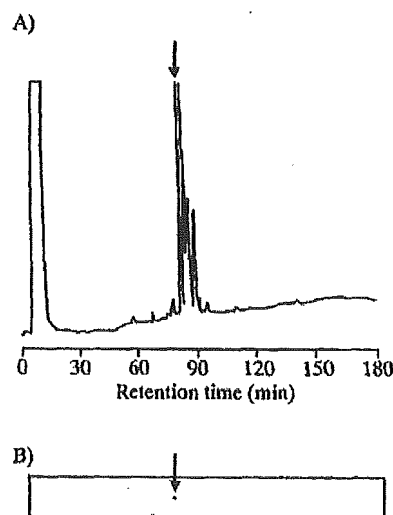
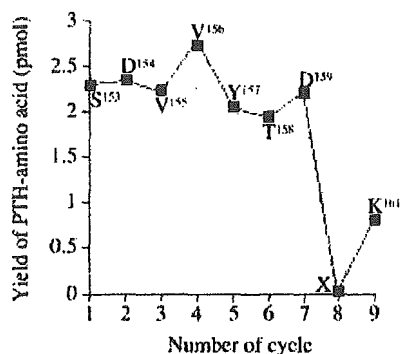


FIG. 6. Chromatogram of capillary HPLC and autoradiogram of blotted PVDF membrane. A, UV-absorption (210 nm). B, autoradiogram of blotted PVDF membrane. After purification of peptides using reverse-phase HPLC, an aliquot of 10  $\mu$ l of the evaporating sample was applied to a  $C_{18}$  column and eluted at 5  $\mu$ l/min using an aqueous acetonitrile gradient in the presence of 0.1% trifluoroacetic acid (from 5 to 95% acetonitrile over the course of 200 min). The blotted membrane from the capillary HPLC separation was in contact with an imaging plate for 48 h prior to autoradiography analysis.

and Lys-161 (Fig. 9B). The surrounding amino acid residues within 5 Å of the UCN-01 molecule include Lys-135, Tyr-157, Trp-160, and Lys-161. The oxygen atom in the sugar ring of



<sup>150</sup>IPKSDVVYTDWKKDKC<sup>165</sup>

FIG. 7. N-terminal amino acid sequence analysis by the Edman degradation method and amino acid sequence of the photolabeled region of hAGP (tryptic peptides). PTH, phenylthiohydantoin.

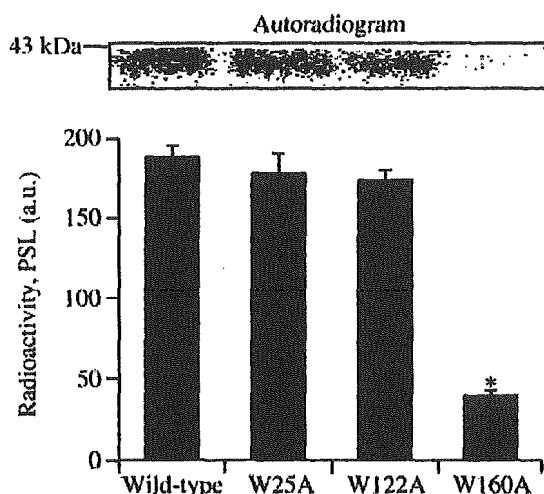


FIG. 8. Photolabeling of wild type, W25A, W122A, and W160A with [<sup>3</sup>H]UCN-01. A sample of 50  $\mu$ M rhAGP was incubated with 0.08  $\mu$ M [<sup>3</sup>H]UCN-01 for 60 min prior to photoirradiation. The samples were separated with 10% SDS-PAGE and electroblotted onto a PVDF membrane for autoradiographic analysis. \*, statistically significant, compared with wild type;  $p < 0.01$ . PSL, photostimulated luminescence.

UCN-01 is in contact with Lys-135. The C=O group of UCN-01 was observed to form a hydrogen bond with the amino group of Trp-160, and electrostatic interaction was observed between the amino group of Lys-161 and both the 7-OH group and C=O group of UCN-01. Furthermore, the aromatic ring of UCN-01 is adjacent to Tyr-157 and Trp-160. In contrast, these interactions were not observed in the type I model, in which UCN-01 was shown to be packed into a surface cleft consisting of Val-41, Glu-43, Ile-44, Phe-48, Tyr-50, Val-156, Thr-158, and Trp-160 (data not shown).

#### DISCUSSION

The acute phase response alters the composition of carrier proteins in plasma, which may affect the blood deposition and transport of biomediators and drugs. Understanding the interaction of drugs with plasma proteins is essential to understanding their systemic pharmacology and toxicology. Thus, information about the effects of the acute phase response on the ligand binding ability of plasma can be used to optimize drug

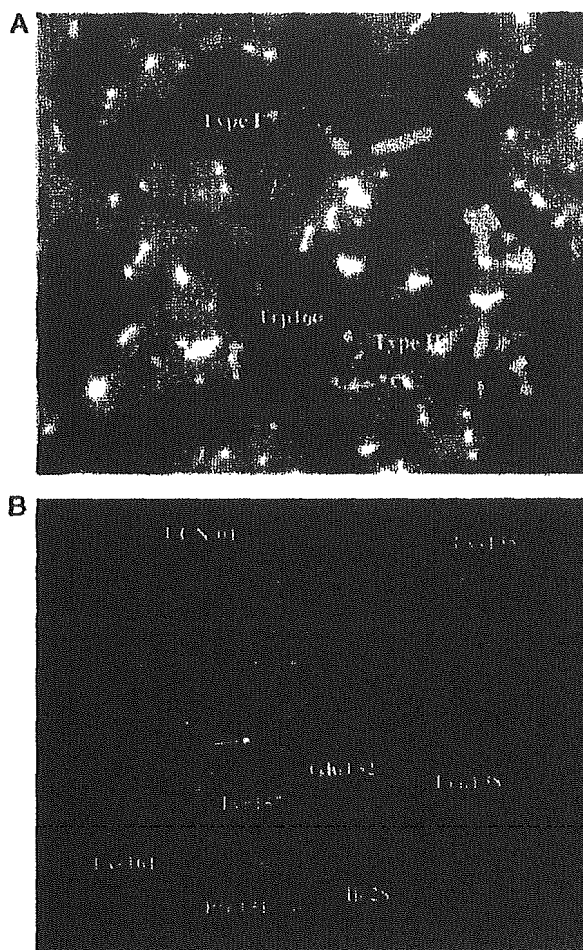


FIG. 9. A, type I and II docking models of UCN-01 and hAGP. Hydrophobic amino acids are shown in green. B, amino acid residues in a surface cleft around Trp-160 that interacts with UCN-01 exhibited in type II docking model. Dotted line, electrostatic interaction. Arrow, hydrogen bonding.

administration protocols in clinical practice. hAGP has been reported to be a major plasma protein that predominantly binds basic drugs (60). However, protein binding studies suggest that hAGP has 1 wide and flexible drug binding area that accommodates not only basic but also acidic and steroidal drugs (61). A current model of the hAGP binding site depicts a buried pocket with a negatively charged region that interacts with the N termini of basic drugs (62). The tertiary structure of hAGP has proven refractory to resolution, and structure-activity studies using various approaches are needed to clarify the nature of the binding site on this important protein.

The initial treatment protocol for UCN-01 was a 72-h infusion administered at 2-week intervals, because certain cell types (e.g. MDA-MB-468 breast carcinoma cells) required 72 h of drug exposure before irreversible growth inhibition occurred (23). However, the clinical outcome of the first 9 patients treated using this schedule demonstrated unexpectedly high concentrations of the drug with a long terminal elimination half-life ( $t_{1/2}$ ). This led to a modification of the UCN-01 administration schedule, in which the recommended phase II dose of UCN-01 is administered as a 72-h continuous infusion at 42.5 mg/m<sup>2</sup>/d over a 3-day period. Second and subsequent courses were administered for only 36 h at the same concentration and

TABLE II  
 Interaction and distance between donors and acceptors in the model of types I and II

Donor	Acceptor	Interaction	Distance Å
Type I			
UCN-01@NH <sub>2</sub>	Glu-43@OE2	Hydrogen bonding	2.793
Tyr-50@OH	UCN-01@C=O	Hydrogen bonding	2.770
Type II			
Trp-160@NE1	UCN-01@C=O	Hydrogen bonding	2.878
Lys-135@NZ	UCN-01@O-	Electrostatic	4.760
Lys-161@NZ	UCN-01@OH	Electrostatic	4.727
Lys-161@NZ	UCN-01@C=O	Electrostatic	4.350
Tyr-157	UCN-01	Stacking	4.204
Trp-160	UCN-01	Stacking	2.878

infusion rate, which effectively reduced the administered dose by 50% for the second and subsequent courses. In addition, the time between courses was increased from 2 weeks to 4 weeks (29). The extremely low clearance and small distribution volume of UCN-01 in humans may be partially caused by its high degree of binding to hAGP (32). Whereas many drugs that associate with hAGP have  $K_a$  values of  $10^5$ – $10^6$  M<sup>-1</sup>, UCN-01 is unique in its high affinity binding to hAGP, and has a  $K_a$  value of  $8 \times 10^8$  M<sup>-1</sup>. The results of this extraordinarily high binding affinity include a low volume of distribution (which approximates the extracellular volume) and long  $t_{1/2}$  (32). The pharmacokinetic effects of the high affinity of UCN-01 for interaction with hAGP indicate that plasma levels of hAGP should be an important consideration in planning of clinical treatment. hAGP has been reported to be a major drug binding plasma protein that interacts mainly with basic drugs (63). Previous studies indicate that hAGP has 1 common drug binding site, which appears to be wide and flexible (61). Characterization of the binding site of UCN-01 on hAGP by Kurata *et al.* (58) revealed partial overlap with amino acid residues implicated in binding of basic drugs, acidic drugs, and steroid hormones. In a previous attempt to further characterize the binding site, we found that Trp-160 is particularly likely to play a major role in the binding of UCN-01. However, because that conclusion was the result of deducing the location of the 3 tryptophan residues, other experimental approaches are needed to confirm it. Currently, no x-ray crystallographic data is available for hAGP, which is a heterogeneous protein consisting of different isoforms and glycosylation states that hinder crystallization. Therefore, in the present study, we examined the possibility of using UCN-01 as a photoaffinity-labeling agent. An ideal photolabeling reagent is stable not only in storage but also under the conditions in which the experiments are performed. Another problem with reagent stability is covalent attachment in the dark, either specific or nonspecific, to the protein under study. All the advantages of photoaffinity labeling are lost if such covalent attachment occurs. In the present study, a covalent bond was formed between UCN-01 and hAGP only upon photoirradiation (Fig. 2).

The results of the present examination of photoinhibition by staurosporine and UCN-02 were as expected (Table I). It is interesting that a change in the configuration of the hydroxyl group of UCN-01 or substitution of a hydrogen atom at the C-7 position of UCN-01 caused a decrease in binding inhibition effects. This confirms our finding that the substituent at C-7 of the UCN-01 molecule governs the affinity of its binding to hAGP. On the other hand, the extensive photoinhibition by progesterone, but not warfarin or propranolol, suggests that the binding site of staurosporine analogs overlaps to a greater extent with the binding site of steroids. This sharing of a binding region between UCN-01 and steroids is thought to be of minimal clinical significance, given the increased hAGP con-

centration in cancer and the extremely high binding affinity of UCN-01 for hAGP.

Sequence analysis of the major radioactive tryptic peptides separated from hAGP photolabeled with [<sup>3</sup>H]UCN-01 showed that these peptides correspond to amino acids Ser-153 to Lys-161 of hAGP. In addition, no phenylthiohydantoin (PTH) derivatives were detected at the 8th cycle, which corresponds to the 160th Trp residue (Fig. 7), indicating that the covalent bond formed upon photolabeling of [<sup>3</sup>H]UCN-01 to hAGP is relatively stable under the conditions of Edman degradation, and that it is highly likely that Trp-160 was photolabeled by [<sup>3</sup>H]UCN-01.

All naturally occurring genetic variants of hAGP conserve the 3 Trp residues in the protein amino acid sequence: Trp-25, Trp-122, and Trp-160 (64). It is noteworthy that there is no significant difference in the binding percentage of UCN-01 between the F1\*S and A variants of hAGP (38). 2 of 3 Trp residues of hAGP are relatively shielded from the bulk solvent, whereas the third Trp residue is located on the periphery of the domain. It has been deduced that Trp-25 is located deep in the binding pocket, and that Trp-122 is located in the central hydrophobic pocket of the protein (65). This suggests that Trp-160 is the Trp residue that is exposed to the bulk solvent. We also used site-directed mutagenesis to identify the key Trp residue involved in UCN-01 binding. Photolabeling of wild-type and mutant rhAGP with [<sup>3</sup>H]UCN-01 revealed that photoincorporation was significantly lower for W160A than for the wild type. In contrast, the level of photoincorporation observed for the other 2 mutants, W25A and W122A, was comparable to that of the wild type. These results strongly support the hypothesis that Trp-160 is the key amino acid responsible for the extraordinarily high affinity of binding between UCN-01 and hAGP.

Previous studies have revealed the structures of UCN-01 and staurosporine bound to the active conformations of Chk1 (47), phospho-CDK2/cyclin A (66), and PDK1 (67). Coincidentally, as observed in the present study, the most important differences previously observed between staurosporine and UCN-01 complexes are the contacts involving the 7-OH group of UCN-01. Komander *et al.* (67) analyzed the relative affinities of staurosporine and UCN-01 for 29 different kinases, and found that binding that was potently inhibited by UCN-01 tended to involve molecules with a side chain that can directly form a hydrogen bond with the 7-OH group of UCN-01. Taking into account the experimental spectra and the unfavorable docking energy, Zsila *et al.* (68) suggested that it is unlikely that curcumin binds inside the central cavity of hAGP. The present docking models show that UCN-01 can interact with surface clefts of hAGP containing Trp-160. The interacting amino acid residues identified by the present type II model are consistent with results of our previous experimental studies of chemical modifications and protein binding (38), as well as those of

present studies using photoaffinity labeling and site-directed mutagenesis.

In order to further analyze the binding cleft of type II docking model, staurosporine and UCN-02, a stereoisomer of UCN-01 with an  $\alpha$ -OH group at the C-7 position, were used to replace UCN-01 at the same position to produce another two docking models (data not shown). In general, all interacting amino acid residues in the two latter models were similar to those of the former, except that the  $\alpha$ -OH group at the C-7 position of UCN-02 interacts with COOH group of Glu-132, in contrast to UCN-01 where the C-7  $\beta$ -OH group interacts with Lys-161. On the other hand, no interaction of any form with the amino acid side chain could be observed for the substituent at C-7 position of staurosporine where hydrogen atom exists. Another amino acid residue that deserved attention was Lys-135 as its distance from the sugar ring of UCN-02 was more than 5 Å, the greatest among the three models.

The following sequence of binding affinity for hAGP has previously been observed: UCN-01 > staurosporine > UCN-02 (38). The aromatic ring of UCN-01 is stacked on Trp-160, and the hydrophobic interaction is strengthened by the electrostatic interaction between the 7-OH group of UCN-01 and Lys-161, which are located on the same side of Trp-160. In contrast, the hydrogen bond between the 7-OH group of UCN-02 and Glu-132, which is located on the opposite side, appears to weaken the hydrophobic interaction, because the ring of UCN-02 has been diverted away from Trp-160. The aromatic ring of staurosporine is not diverted from Trp-160, due to the absence of the 7-OH group. In order to gain deeper insight on the binding mechanism of UCN-01 to hAGP, experiments using Glu-132 and Lys-161 hAGP mutants to examine the role of each mutated amino acid residue in the high affinity binding of UCN-01 is currently underway in our laboratory.

Staurosporine is a natural product derived from fermentation extracts of several bacterial species. Staurosporine was initially identified as a potent inhibitor of PKC, which is a  $\text{Ca}^{2+}$ - and phospholipid-activated kinase (69). Different isoforms of PKC are activated in response to growth factors that act on receptor tyrosine kinases and 7-transmembrane domain receptors (70). Studies have revealed that staurosporine is a broad-acting kinase inhibitor with little specificity or selectivity for PKC (71). Recently, the staurosporine analog *N*-benzoyl-staurosporine (PKC412) has been reported to exhibit strong hAGP binding, and to have unusual pharmacokinetics similar to those of staurosporine, which were not predicted by animal studies (72). PKC412 is the only staurosporine inhibitor of protein kinases other than UCN-01 that has been subjected to a clinical trial. There has been a study of oral administration of PKC412 once daily (73). It is interesting that PKC412 exhibits complex pharmacology resulting from binding to hAGP. Preclinical experiments had shown extensive binding of PKC412 to human plasma proteins, with ~88–98% protein binding, depending on the drug concentration (72). Rates of binding of PKC412 to hAGP were particularly interesting. In the preclinical experiments, the plasma concentrations of PKC412 were higher, and the half-life was longer than predicted from animal studies and single dose kinetics studies with healthy volunteers (72). In contrast to UCN-01, PKC412 was metabolized to 7-hydroxy-PKC412 and an *O*-demethyl-PKC412, both of which also bound to hAGP. The major metabolite had a particularly long half-life (74). It is possible that PKC412 and its metabolite preferentially bind to hAGP *in vivo*, and this may account for the longer than anticipated plasma half-life. The dynamics of dissociation of PKC412 from plasma proteins and tissue distribution of PKC412 are likely to be complex, and plasma levels may not accurately reflect drug concentration in target tissues.

Because plasma pharmacokinetic evaluation is complicated by protein binding and metabolism, studies using biologic markers of PKC inhibition can contribute to optimization of PKC412 administration.

#### CONCLUSIONS

Because of the potential implications of species-specific binding of UCN-01 to hAGP in human plasma for the development of staurosporine analogs, studies of analogs of UCN-01 and of PKC412, which lack hAGP binding or very weakly bind to hAGP, should be conducted along with studies of the potential usefulness of staurosporine pharmacophores. Characterization of the binding site of UCN-01 on hAGP using photoaffinity labeling and site-directed mutagenesis techniques has provided direct evidence that strongly indicates that Trp-160 plays an important role in the binding interaction between UCN-01 and hAGP. In addition to the obvious pharmacokinetic implications of the extraordinarily high affinity of binding of UCN-01 to hAGP, the present results suggest that hAGP is a suitable platform for further design of novel staurosporine analog anticancer drugs, and also for evaluation of side effects and drug interaction in clinical settings. The present results provide clues to the design of future second-generation therapeutic agents, and can serve as a basis for future studies of UCN-01 administered alone and in combination with other anticancer drugs, particularly DNA-damaging agents.

*Acknowledgment*—We thank Dr. Vladimír Kopecký, Jr. of the Institute of Physics, Charles University in Prague, for providing us with the protein moiety of hAGP in the native state and with docked progesterone in a PDB format.

#### REFERENCES

- Schmid, K., Nimerg, R. B., Kimura, A., Yamaguchi, H., and Binette, J. P. (1977) *Biochim. Biophys. Acta* 492, 291–302
- Kramer, J. M., Wiltling, J., and Janssen, L. H. (1988) *Pharmacol. Rev.* 40, 1–47
- Van Dijk, W. (1995) *Adv. Exp. Med. Biol.* 376, 223–229
- Hochepied, T., Berger, F. G., Baumann, H., and Libert, C. (2003) *Cytokine Growth Factor Rev.* 14, 25–34
- Cheresh, D. A., Haynes, D. H., and Distasio, J. A. (1984) *Immunology* 51, 541–548
- Morita, K., and Yamaji, A. (1995) *Theor. Drug Monit.* 17, 107–112
- Mackiewicz, A., and Mackiewicz, K. (1995) *Glycoconj. J.* 12, 241–247
- Duche, J. C., Urien, S., Simon, N., Malaurio, E., Monnet, I., and Barre, J. (2000) *Clin. Biochem.* 33, 197–202
- Fan, C., Standahl, U., Sjöberg, N., and Beckman, I. (1995) *Oncology* 52, 498–500
- Mazoit, J. X., and Dalens, B. J. (2004) *Clin. Pharmacokinet.* 43, 17–32
- Veering, B. T., Borm, A. G., Feyen, H. M., Olieman, W. M., Souverijn, J. H., and Van Kleef, J. W. (2002) *Anesthesiology* 96, 1062–1069
- Hedaya, M. A., and Daoud, S. S. (2001) *Anticancer Res.* 21, 4005–4010
- Gambacurti-Passerini, C., Zucchetti, M., Russo, D., Frapolli, R., Vergo, M., Bungaro, S., Tornaghi, L., Rossi, F., Pioltelli, P., Pogliani, E., Alberti, D., Corneo, G., and D'Incalci, M. (2003) *Clin. Cancer Res.* 9, 625–632
- Bruno, R., Olivares, R., Berille, J., Chaikin, P., Vivier, N., Hammershaimb, L., Rhodes, G. R., and Rigus, J. R. (2003) *Clin. Cancer Res.* 9, 1077–1082
- Takahashi, I., Kobayashi, E., Asano, K., Yoshida, M., and Nakano, H. (1987) *J. Antibiot. (Tokyo)* 40, 1782–1784
- Penuelas, S., Alemany, C., Noe, V., and Ciudad, C. J. (2003) *Eur. J. Biochem.* 270, 4809–4822
- Yu, Q., La, Rose, J., Zhang, H., Takemura, H., Kohn, K. W., and Pommier, Y. (2002) *Cancer Res.* 62, 5743–5748
- Facchinetti, M. M., De, Siervi, A., Toskos, D., and Senderowicz, A. M. (2004) *Cancer Res.* 64, 3629–3637
- Dai, Y., Pei, X. Y., Bahmani, M., Conrad, D. H., Dent, P., and Grant, S. (2004) *Blood* 103, 2761–2770
- Tenzler, A., and Proschy, M. (2003) *Curr. Med. Chem. Anti-Cancer Agents* 3, 35–46
- Akinaga, S., Gomi, K., Morimoto, M., Tamaki, T., and Okabe, M. (1991) *Cancer Res.* 51, 4898–4899
- Akinaga, S., Nomura, K., Gomi, K., and Okabe, M. (1994) *Cancer Chemother. Pharmacol.* 33, 273–280
- Seynueve, C. M., Steller-Stevenson, M., Sebers, S., Kaur, G., Sausville, E. A., and Worland, P. J. (1993) *Cancer Res.* 53, 2081–2086
- Senderowicz, A. M. (2003) *Oncogene* 22, 6609–6620
- Akiyama, T., Yoshida, T., Tsujita, T., Shimizu, M., Mizukami, T., Okabe, M., and Akinaga, S. (1997) *Cancer Res.* 57, 1495–1504
- Akinaga, S., Nomura, K., Gomi, K., and Okabe, M. (1993) *Cancer Chemother. Pharmacol.* 32, 183–189
- Abe, S., Kubota, T., Otani, Y., Furukawa, T., Watanabe, M., Kumai, K., and Kitajima, M. (2000) *Jpn. J. Cancer Res.* 91, 1192–1198
- Bunch, R. T., and Eastman, A. (1996) *Clin. Cancer Res.* 2, 791–797

29. Sausville, E. A., Arbuch, S. G., Messmann, R., Headlee, D., Bauer, K. S., Lush, R. M., Margo, A., Figg, W. D., Lahusen, T., Jaken, S., Jing, X., Roberge, M., Fuse, E., Kuwabara, T., and Senderowicz, A. M. (2001) *J. Clin. Oncol.* **19**, 2319-2333
30. Senderowicz, A. M. (2002) *Hematol. Oncol. Clin. North Am.* **16**, 1229-1263
31. Fuse, E., Tani, H., Takui, K., Asanome, K., Kurata, N., Kobayashi, H., Kuwabara, T., Kobayashi, S., and Sugiyama, Y. (1999) *Cancer Res.* **59**, 1054-1060
32. Fuse, E., Tani, H., Kurata, N., Kobayashi, H., Shimada, Y., Tamura, T., Sasaki, Y., Tanigawara, Y., Lush, R. D., Headlee, D., Figg, W. D., Arbuch, S. G., Senderowicz, A. M., Sausville, E. A., Akinaga, S., Kuwabara, T., and Kobayashi, S. (1998) *Cancer Res.* **58**, 3248-3253
33. Sausville, E. A., Lush, R. D., Headlee, D., Smith, A. C., Figg, W. D., Arbuch, S. G., Senderowicz, A. M., Fuse, E., Tani, H., Kuwabara, T., and Kobayashi, S. (1998) *Cancer Chemother. Pharmacol.* **42**, 54-59
34. Bailey, D. N., and Briggs, J. R. (2004) *Ther. Drug Monit.* **26**, 40-43
35. Nakai, D., Kumamoto, K., Sakikawa, C., Kosuka, T., and Tokui, T. (2004) *J. Pharm. Sci.* **93**, 847-854
36. Kute, T., and Westphal, U. (1976) *Biochim. Biophys. Acta* **420**, 195-213
37. Haughey, D. B., Steinberg, I., and Lee, M. H. (1985) *J. Pharm. Pharmacol.* **37**, 285-288
38. Katsuki, M., Chuang, V. T. G., Nishi, K., Suenaga, A., and Otagiri, M. (2004) *Pharm. Res.* **21**, 1648-1655
39. Hatanaka, Y., and Sadakane, Y. (2002) *Curr. Top. Med. Chem.* **2**, 271-288
40. Chang, S. H., and Low, P. S. (2003) *J. Biol. Chem.* **278**, 6879-6884
41. Sato, T., Shimada, Y., Nagasawa, N., Nakanishi, S., and Jingami, H. (2003) *J. Biol. Chem.* **278**, 4314-4321
42. Nishi, K., Fukunaga, N., and Otagiri, M. (2004) *Drug Metab. Dispos.* **32**, 1069-1074
43. Braman, J., Papworth, C., and Greener, A. (1996) *Methods Mol. Biol.* **57**, 31-44
44. Zor, T., and Selinger, Z. (1996) *Anal. Biochem.* **236**, 302-308
45. Davis, M. T., and Lee, T. D. (1992) *Protein Sci.* **1**, 935-944
46. Kopecky, V. Jr., Eltrich, R., Hofbauerova, K., and Baumruk, V. (2003) *Biochem. Biophys. Res. Commun.* **300**, 41-46
47. Zhao, B., Bower, M. J., McDevitt, P. J., Zhao, H., Davis, S. T., Johanson, K. O., Green, S. M., Concha, N. O., and Zhou, B. B. (2002) *J. Biol. Chem.* **277**, 46609-46615
48. Rarey, M., Kramer, B., Lengauer, T., and Klebe, G. (1996) *J. Mol. Biol.* **261**, 470-489
49. Jones, G., Willett, P., Glen, R. C., Leach, A. R., and Taylor, R. (1997) *J. Mol. Biol.* **287**, 727-748
50. Muegge, I., and Martin, Y. C. (1999) *J. Med. Chem.* **42**, 791-804
51. Kuntz, I. D., Blaney, J. M., Oatley, S. J., Langridge, R., and Ferrin, T. E. (1982) *J. Mol. Biol.* **161**, 269-288
52. Eldridge, M. D., Murray, C. W., Auton, T. R., Paolini, G. V., and Mee, R. P. (1997) *J. Comput. Aided Mol. Design* **11**, 425-445
53. Carnell, W. D., Cieplak, P., Bayly, C. I., Gould, I. R., Merz, K. M., Jr., Ferguson, D. M., Spellmeyer, D. C., Fox, T., Caldwell, J. W., and Kollman, P. A. (1995) *J. Am. Chem. Soc.* **117**, 5179-5197
54. Gasteiger, J., and Marsili, M. (1980) *Tetrahedron* **36**, 3219-3228
55. Gasteiger, J., and Marsili, M. (1981) *Organ. Magn. Reson.* **15**, 353-360
56. Marsili, M., and Gasteiger, J. (1980) *Croat. Chem. Acta* **53**, 601-614
57. Purcell, W. P., and Singer, J. A. (1967) *J. Chem. Eng. Data* **12**, 235-246
58. Kurata, N., Matsushita, S., Nishi, K., Watanabe, H., Kobayashi, S., Suenaga, A., and Otagiri, M. (2000) *Biol. Pharm. Bull.* **23**, 893-895
59. Urien, S., Giroud, Y., Tsai, R. S., Carrupt, P. A., Bree, F., Testa, B., and Tillement, J. P. (1995) *Biochem. J.* **306**, 545-549
60. Israili, Z. H., and Duyton, P. G. (2001) *Drug Metab. Rev.* **33**, 161-235
61. Miyoshi, T., Yamamichi, R., Maruyama, T., Takadate, A., and Otagiri, M. (1992) *Biochem. Pharmacol.* **43**, 2161-2167
62. Taheri, S., Cogswell, L. P., 3rd., Gent, A., and Strichartz, G. R. (2003) *J. Pharmacol. Exp. Ther.* **304**, 71-80
63. Routledge, P. A. (1986) *Br. J. Clin. Pharmacol.* **22**, 499-506
64. Deute, L., Pizsa, M. G., Metspalu, A., and Cortese, R. (1987) *EMBO J.* **6**, 2289-2296
65. Friedman, M. L., Schlueter, K. T., Kirley, T. L., and Halsall, H. B. (1985) *Biochem. J.* **232**, 863-867
66. Johnson, L. N., De Moliner, E., Brown, N. R., Song, H., Barford, D., Endicott, J. A., and Noble, M. E. (2002) *Pharmacol. Ther.* **93**, 113-124
67. Komander, D., Kular, G. S., Bain, J., Elliott, M., Alessi, D. R., and Van Aalten, D. M. (2003) *Biochem. J.* **375**, 265-262
68. Zsila, F., Bikadi, Z., and Simonyi, M. (2004) *Bioorg. Med. Chem.* **12**, 3239-3245
69. Tamaoki, T., Nomoto, H., Takahashi, I., Kato, Y., Morimoto, M., and Tomita, F. (1986) *Biochem. Biophys. Res. Commun.* **135**, 397-402
70. Rodriguez-Fernandez, J. L., and Rozengurt, E. (1998) *J. Biol. Chem.* **273**, 19321-19328
71. Katira, A., Knox, K. A., Finney, M., Michell, R. H., Wakelam, M., and Gordon, J. (1993) *Clin. Exp. Immunol.* **92**, 347-352
72. Propper, D. J., McDonald, A. C., Mau, A., Thavasu, P., Balkwill, F., Braybrooke, J. P., Capomigro, F., Graf, P., Dutreix, C., Blackie, R., Kaye, S. B., Ganesan, T. S., Talbot, D. C., Harris, A. L., and Twelves, C. (2001) *J. Clin. Oncol.* **19**, 1485-1492
73. Monnerat, C., Henriksson, R., Le, Chevalier, T., Novello, S., Berthaud, P., Faivre, S., and Raymond, E. (2004) *Ann. Oncol.* **15**, 316-323
74. Eder, J. P., Jr., Garcia-Carbonero, R., Clark, J. W., Supko, J. G., Puchalski, T. A., Ryan, D. P., Deluca, P., Wozniak, A., Campbell, A., Rothmell, J., and LoRusso, P. (2004) *Investig. New Drugs* **22**, 139-150

# New AMBER Force Field Parameters of Heme Iron for Cytochrome P450s Determined by Quantum Chemical Calculations of Simplified Models

AKIFUMI ODA,<sup>1</sup> NORIYUKI YAMAOTSU,<sup>2</sup> SHUICHI HIRONO<sup>2</sup>

<sup>1</sup>Discovery Laboratories, Toyama Chemical Co., Ltd., 2-4-1 Shimookui,  
Toyama 930-8508, Japan

<sup>2</sup>School of Pharmaceutical Sciences, Kitasato University, 5-9-1 Shirokane, Minato-ku,  
Tokyo 108-8641, Japan

Received 24 September 2004; Accepted 20 December 2004

DOI 10.1002/jcc.20221

Published online 6 April 2005 in Wiley InterScience (www.interscience.wiley.com).

**Abstract:** The heme protein, cytochrome P450, is an oxidoreductase that plays an important role in drug metabolism. To model P450s using molecular mechanics methods and classical molecular dynamics simulations, force field parameters and atomic charges are required. Because these parameters are generally obtained by quantum chemical methods, an appropriate simplified model for the iron–porphyrin system was needed. In this study, two models with a five-coordinated Fe(III) mimicking the sextet spin state of P450s are proposed, which are optimized by semiempirical and *ab initio* unrestricted Hartree–Fock methods. The results produced using the simpler of the two models were similar to those of the more complex model; therefore, the more simplified model of P450 can be used without a loss of accuracy. Furthermore, several quantum chemical calculations were carried out on the simpler model to investigate which method was most suitable for iron–porphyrin systems. The results calculated by hybrid density functional theory (DFT), with the MIDI basis set for iron, reproduced the three-dimensional structures determined by X-ray diffraction and extended X-ray absorption fine-structure experiments. From these results, atomic charges and force-field parameters for molecular mechanics and molecular dynamics calculations were obtained.

© 2005 Wiley Periodicals, Inc. J Comput Chem 26: 818–826, 2005

**Key words:** AMBER force-field; atomic charge; cytochrome P450; DFT; iron–porphyrin

## Introduction

Cytochrome P450 is a family of oxidoreductases with a wide variety of substrates, and is among the most important enzymes for metabolism within the living body. P450s metabolize both endogenous and exogenous substrates. Steroids,<sup>1</sup> arachidonic acid,<sup>2,3</sup> and retinoid<sup>4,5</sup> are all reported to be endogenous substrates of these enzymes. Metabolites from these substrates have important biological functions; therefore, P450 proteins play a significant role in maintaining the homeostasis of the living body. They also metabolize exogenous substrates, such as drugs and toxic agents, and are responsible for the metabolic activation of exogenous mutagenic compounds. Around 20 P450s have been reported to play important roles in drug metabolism in humans<sup>6</sup> and to metabolize a variety of different drugs.<sup>7</sup> Polymorphisms in some important P450s, for example, CYP2C9, CYP2C19, and CYP2D6, are responsible for differing drug metabolism between individuals.<sup>8</sup> Therefore, investigating whether a specific drug inhibits and/or is metabolized by P450s is desirable in drug design studies.

P450s are monooxygenases that include a heme moiety axially ligated to a cysteinyl (CYS) sulfur. Catalytic reactions occur at the iron center of heme, and P450s generally insert an oxygen atom into hydrophobic molecules between the carbon and hydrogen atoms of a C–H bond or the two carbon atoms of a C–C bond. The catalytic cycle of P450s is illustrated in Figure 1. The oxidation state of the heme iron (Fe(II) or Fe(III)), the spin state (high- or low-spin) and the number of ligands (five- or six-coordinated) all play important roles in this cycle.<sup>9</sup> In the first step, the heme iron is low-spin six-coordinated Fe(III). A water molecule is at the coordination position *trans* to the CYS. Upon substrate docking, the water ligand is unbound from the iron atom. Substrate binding

Correspondence to: A. Oda; e-mail: AKIFUMI\_ODA@toyama-chemical.co.jp

This article includes Supplementary Material available from the authors upon request or via the internet at <http://www.interscience.wiley.com/jpages/0192-8651/suppmat>

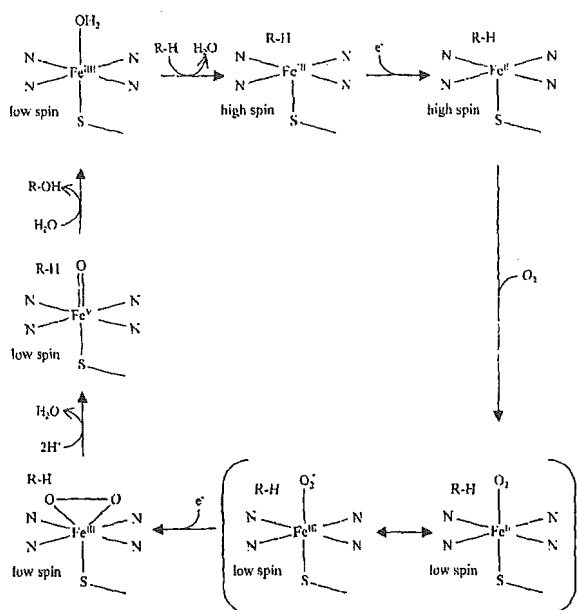


Figure 1. Catalytic cycle of P450s.

leads to an increase in the redox potential and, therefore, the enzyme can accept an electron from an electron-donor molecule such as NADPH or NADH. Fe(III) is thus reduced to Fe(II) and the catalytic reaction proceeds to the next step of the cycle. Substrate binding also generally causes a shift from a low- to a high-spin state. In P450cam from *Pseudomonas putida*, which metabolizes camphor, the redox potential increases from  $-300$  mV to  $-173$  mV on substrate binding.<sup>10</sup>

As previously mentioned, because high-spin five-coordinated Fe(III) is closely related to substrate binding, computational evaluation of this state is important in studies of the drugs and toxic agents that are docked into P450 enzymes. Recently, several iron-porphyrin complex models of P450s have been built using quantum chemistry methods. Complex models with six-coordinated iron,<sup>11-13</sup> and models with substrates or inhibitors, such as alkane, alkene, and nitric oxide,<sup>14-18</sup> have been examined using various computational methods, including Hartree-Fock calculations<sup>19</sup> and density functional theories.<sup>11-18,20</sup> However, there have been few studies on iron-porphyrin models with high-spin state five-ligated Fe(III).<sup>19,20</sup> Furthermore, there has been no systematic study of these five-coordinated Fe(III) iron-porphyrin models using different methods and basis sets.

To investigate the interaction between P450s and various small compounds in drug design trials, molecular mechanical (MM) calculations and classical molecular dynamics (CMD) simulations are generally suitable in terms of time and costs. Although simplified models are important for detailed investigations of the chemical properties of proteins, whole protein structures that are not simplified are indispensable in drug design investigations, such as docking studies on small molecules, virtual screening trials, and *de novo* design. Several quantum chemical methods and QM/MM

methods for whole proteins have been developed,<sup>21-23</sup> but they are too computationally expensive to investigate large numbers of protein-ligand complexes, for example, in virtual screening. Therefore, MM and CMD calculations are the most suitable methods for drug design and development. Force field parameters are indispensable in MM and CMD methods, and parameters for molecules other than amino acids, such as heme, are often unavailable. Although sets of force field parameters for the heme moiety are available (<http://pharmacy.man.ac.uk/amber/>),<sup>24</sup> they are intended for calculations of hemoglobin, myoglobin, and cytochrome *c*, and are therefore not suitable for P450s. These parameters can be used for porphyrin rings, but parameters relating to axial ligands of the iron atom (that is, CYS) have not yet been determined. Furthermore, parameters only exist for heme with a six-ligated iron atom and those for heme with a five-coordinated iron atom, which plays an important role in the catalytic cycle of P450s, remain to be calculated. In addition to force field parameters, atomic charges are generally required for MM and CMD, and the electronic states need to be investigated in order to calculate these values.

Quantum chemical calculations with simplified models are generally used to determine parameters and atomic charges for MM and CMD. The results of quantum chemical calculations on iron-porphyrin simplified models can be used in MM and CMD calculations on whole P450s. In this way, it is possible to predict substrate binding modes and complete virtual screening trials for drug candidates. High-spin state five-ligated Fe(III), which is related to substrate binding, plays a significant role in these calculations.

In this study, models with five-coordinated Fe(III) are built for P450s and their accuracies are evaluated using geometry optimizations via various quantum chemical methods. Furthermore, we investigate which methods are most suitable for use with these models. The parameters and atomic charges that are indispensable in MM and MD calculations for P450s are also obtained.

## Methods

The iron-porphyrin models used in this study are illustrated in Figure 2. Model 1 is a detailed model of a P450 enzyme, which includes the protoporphyrin IX with Fe(III) axially ligated through the sulfur atom of CYS. An acetyl group (ACE) and a methylamino group (NME) are bound to the amino (N)- and carboxy (C)-terminuses of CYS, respectively. Model 2 is more simplified and includes the porphyrin with Fe(III) axially ligated to the sulfur of a methylthio group. There are 95 and 42 atoms in models 1 and 2, respectively.

For each model, geometry optimizations were carried out using the following quantum chemical methods: semiempirical unrestricted Austin Model 1 (AM1); *ab initio* unrestricted Hartree-Fock (UHF) molecular orbital methods; and unrestricted hybrid density functional theory (DFT) combining five functionals—Hartree-Fock, Slater, and Becke exchange, and Vosko-Wilk-Nusair and Lee-Yang-Parr correlation terms (UB3LYP). 3-21G\*, 4-31G\*, 6-31G\*, and Tatewaki-Huzinaga's MIDI<sup>25</sup> with Hay's diffuse  $d^{26}$  basis sets were adopted. A different basis set was used for the iron atom in some of the calculations. Table 1 shows the



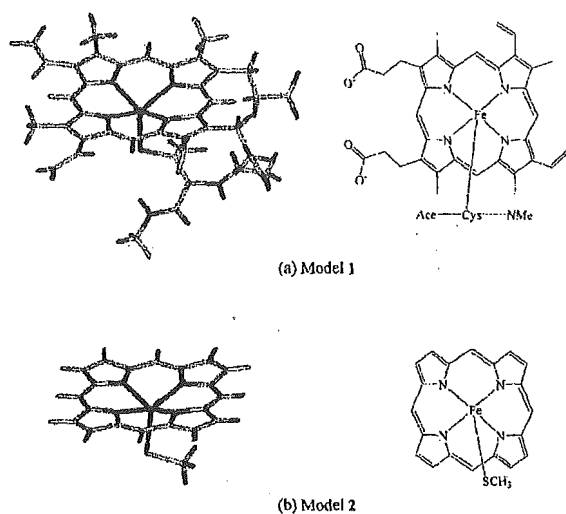


Figure 2. Two models of P450s used in this study.

combination of quantum chemical methods and basis sets used for each model.

The atomic charges necessary for MM and CMD methods were calculated from the optimized structure. To apply these charges in calculations using whole P450s, atomic charges were computed for the more complex model 1 using method III. Various techniques for atomic charge calculations using quantum chemical methods have been proposed.<sup>27-31</sup> This study used RESP method,<sup>30,31</sup> which is a modified version of Merz-Kollman method<sup>29</sup> that is known to generate suitable charges for MM and CMD. RESP charge is obtained to reproduce the electrostatic potential and is recommended for AMBER,<sup>32</sup> which is one of the most widely used CMD programs. In AMBER program, total charges of amino acid residues are defined as integer values when the ACE and

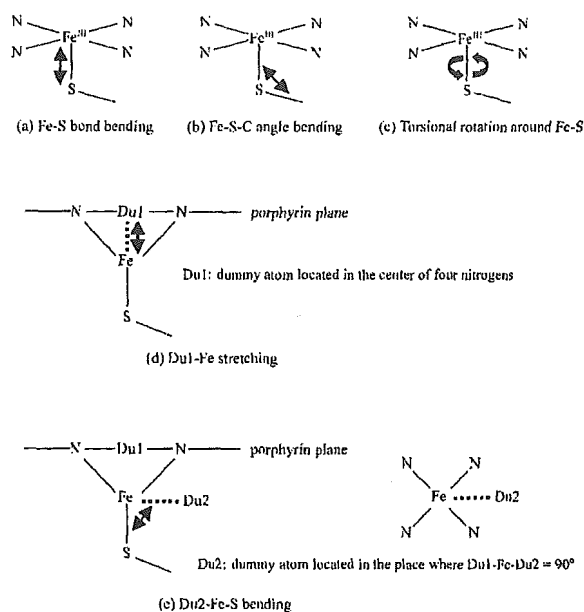


Figure 3. Structural changes to calculate energy profiles for the parameterization of P450s.

NME groups are removed.<sup>31</sup> Therefore, the total charge of model 1 was defined as  $-2$  when the ACE and NME were removed. The previously defined values of atomic charges for ACE and NME were used.<sup>31</sup>

Model 2 was used to calculate the force field parameters. As shown in Figure 3, energy changes with Fe-S bond bending, Fe-S-C angle bending and torsional motion around Fe-S were calculated using quantum chemical methods, and parameter fitting was carried out using calculated energy profiles. In addition to

Table 1. Quantum Chemical Methods Used in This Study.

(a) Model 1									
	I				III				
Method	AM1				UHF				
Basis sets for H, C, N, O and S	AM1				3-21G*				
Basis sets for Fe(III)	AM1				MIDI <sup>a</sup>				
(b) Model 2									
	i	ii	iii	iv	v	vi	vii	viii	ix
Method	AM1	UHF	UHF	UHF	UHF	UHF	UHF	UB3LYP	UB3LYP
Basis sets for H, C, N and S	AM1	3-21G*	3-21G*	4-31G*	4-31G*	6-31G*	6-31G*	4-31G*	4-31G*
Basis sets for Fe(II)	AM1	3-21G*	MIDI <sup>a</sup>	6-31G*	MIDI <sup>a</sup>	6-31G*	MIDI <sup>a</sup>	6-31G*	MIDI <sup>a</sup>

<sup>a</sup>Tatcawaki-Huzinaga MIDI plus Hay's diffuse basis sets.

parameters around Fe—S, parameters for interactions between iron and porphyrin were also determined to reproduce the location of the iron atom, which is out of porphyrin plane in high-spin state. To calculate these parameters, only Fe—SCH<sub>3</sub> moiety was moved along Du1—Fe (Du1 was a dummy atom located in the center of four nitrogen atoms) and Du2—Fe—C (Du2 was a dummy atom located in the place where angle Du1—Fe—Du2 is equal to 90°) as shown in Figure 3d and c, respectively, and the energy profiles were calculated. For this purpose, the least-square method was performed to minimize the standard deviation (SD) in eq. (1),

$$SD = \sum (E(QC) - E(MM))^2 \quad (1)$$

where  $E(QC)$  is the energy calculated through quantum chemical methods and  $E(MM)$  is obtained using the force field. These calculations used UB3LYP with the M11D basis sets for iron and 4-31G\* for other elements. PARM94 parameters<sup>33</sup> [eq. (2)] in AMBER were adopted as the force field,

$$E_{\text{total}} = \sum_{\text{bonds}} K_r (r - r_{\text{eq}})^2 + \sum_{\text{angles}} K_{\theta} (\theta - \theta_{\text{eq}})^2 + \sum_{\text{dihedrals}} \frac{V_n}{2} [1 + \cos(n\phi - \gamma)] + \sum_{i < j} \left( \frac{A_{ij}}{R_{ij}^{12}} - \frac{B_{ij}}{R_{ij}^6} + \frac{q_i q_j}{\epsilon R_{ij}} \right) \quad (2)$$

where the first and second terms, which are related to bond stretching and angle bending, respectively, express the harmonic-oscillator approximations. The parameters  $r_{\text{eq}}$  and  $\theta_{\text{eq}}$  are equilibrium bond length and bond angle, and  $K_r$  and  $K_{\theta}$  are force constants. The third term is the torsional term, where  $V_n$  is the energy barrier of torsional motion,  $n$  is the periodicity and  $\gamma$  is the phase. The last term describes nonbonded interactions. In this study, AMBER PARM94 and Giammona's parameters (<http://pharmacy.man.ac.uk/amber/>) were used to calculate the energies of iron-porphyrin systems, with the exception of parameters around iron atom.

To validate the parameters obtained, MM calculations of P450cam with five-coordinated Fe(III) were carried out and the structures were compared before and after the calculations. The experimental crystal structure determined by X-ray diffraction (PDB ID: 2CPP)<sup>34</sup> was used for the initial structure of P450cam. Because hydrogen atoms were not determined in this experimental structure, they were added by using the "Protonate" module of AMBER 6.<sup>32</sup> Furthermore, the side-chain atoms of Lys214, which were missing in the crystal structure, were added using the "Biopolymer" module of SYBYL6.9.2.<sup>35</sup> In the first step of the MM calculation on P450cam, only the added hydrogens and side-chain atoms were optimized. An MM optimization of all atoms in P450cam was then carried out. For all MM calculations, the first 1000 steps were completed using the steepest-descent method, and the rest of the calculation was carried out using the conjugate-gradient method until the energy gradient became less than 0.01 kcal/mol Å. A cutoff distance of 18.0 Å for nonbonded interactions and a constant dielectric coefficient of  $\epsilon = 77.9$  were used in the refinement.

AM1 calculations were carried out using MOPAC2002.<sup>36</sup> UHF and UB3LYP calculations were performed using Gaussian98.<sup>37</sup>

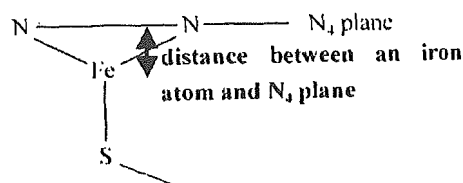


Figure 4. Distance between iron atom and N<sub>4</sub> plane.

The calculation of RESP charges and the MM calculations on P450cam, carried out to validate the force field parameters around Fe—S, were completed using AMBER 6.<sup>32</sup> An SGI OCTANE workstation with MIPS R12000 dual processors and IRIX 6.5 were used.

## Results and Discussions

After optimization using the same methods, the structures of models 1 and 2 were compared. Some of the bond lengths, bond angles, and distances between the iron atom and N<sub>4</sub> plane (illustrated in Fig. 4) are shown in Table 2 (Other bond length and bond angles are illustrated in Supplementary Material). In addition to the computational results, experimentally determined structures for high-spin state P450, homologous enzyme, and model compounds with five-coordinated Fe(III) are also described. Four experimental results are mentioned: EXAFS 1, which is the structure of P450cam using extended X-ray-absorption fine structure (EXAFS);<sup>38</sup> EXAFS 2, which is the structure of chloroperoxidase from EXAFS;<sup>39</sup> X-ray 1, which is the structure of P450cam by X-ray diffraction;<sup>34</sup> and X-ray 2, which is the structure of Fe(PPIXDMF)(SC<sub>6</sub>H<sub>4</sub>NO<sub>2</sub>) by X-ray crystallography.<sup>40</sup> Computationally determined bond lengths are compared in Figure 5. As the tables and the figures show, all of the structural features were similar between model 1 and 2, with the exception of bond lengths and angles related to the iron atom obtained by AM1. Using UHF methods, the differences in bond length between the two models were within 10<sup>-2</sup> Å, with the exception of Fe—S bond length, and the differences in bond angles were all within 1°. The structural differences calculated by AM1 methods without structural features near the iron atom were similar to the UHF results. These results suggest that the more simplified model 2 is sufficiently accurate to calculate the structural features of iron-porphyrin systems. Because the numbers of atoms in models 1 and 2 were 95 and 42, respectively, the use of the latter for quantum calculations would reduce computational time and costs. The results of the superposition of the two models are illustrated in Figure 6. The root-mean-square deviations (RMSDs) of the porphyrin moieties between the two models were calculated as 0.142 Å and 0.068 Å using the AM1 and UHF methods, respectively. If experimental structure determination is repeated on the same protein, experimental error and the dynamic nature of proteins leads to RMSDs of approximately 0.4 Å.<sup>41</sup> In comparison, the RMSDs from these computationally optimized structures are small. These results also indicate that model 2 would be suitable for investigations into the structural features of P450s.

Table 2. Optimized Structures of Model 1 and 2.

(a) Bond lengths around Fe/Å								
Method	EXAFS 1	EXAFS 2	X-ray 1	X-ray 2	I	i	III	iii
Fe—S	2.23	2.30	2.20	2.324	2.209	2.242	2.532	2.482
Fe—N	2.06	2.05	2.05	2.064	2.114	2.038	2.170	2.163
(b) Bond angles around Fe/deg								
Method	X-ray 1	X-ray 2	I	i	III	iii		
$N_{\alpha}-Fe-N_{\nu}$	155.6	155.7	152.7	167.0	145.2	144.7		
$N_{\alpha}-Fe-N_{\beta}$	87.4	87.5	86.8	89.3	84.9	84.7		
(c) Distances between $N_4$ plane and Fe/Å								
Method	X-ray 1	X-ray 2	I	i	III	iii		
$N_4-Fe$	0.43	0.434	0.498	0.231	0.648	0.655		

The structures of model 1 and 2 optimized by AM1 and UHF are compared with experimental structures.

Following on from the results mentioned previously, geometry optimizations of model 2 were carried out using more accurate methods. The results are shown in Table 3, in which some of bond lengths, bond angles, and distances between the  $N_4$  plane and the iron atom are described in the same way as in Table 2 (other structural features were shown in Supplementary Material). For structural features not related to the iron atom, almost all of the computational results reproduced the experimental results, with only a few exceptions when using methods ii and iii. However, for structural features around the iron atom, none of the UHF methods gave reasonable results compared with the experimental data. These results indicate that the UHF method is inadequate for

quantum chemical elucidation of P450 structures. Although method vii required a much longer time to complete the calculation than method v, the structural features calculated using methods v and vii were similar. In fact, method v occasionally gave better results than method vii (e.g., the results for the bond length of  $C_{\alpha}-C_{\beta}$ ). Fast and accurate calculations are desirable for the preparation of MM and CMD, because many calculations are required to obtain energy profiles. Therefore, the 4-31G\* basis set seems to be more suitable for H, C, N, and S atoms than 6-31G\*.

The AM1 method produced reasonable values for Fe—S and Fe—N bond lengths, which indicates that AM1-d parameters are effective in calculating bond lengths. However, despite this find-

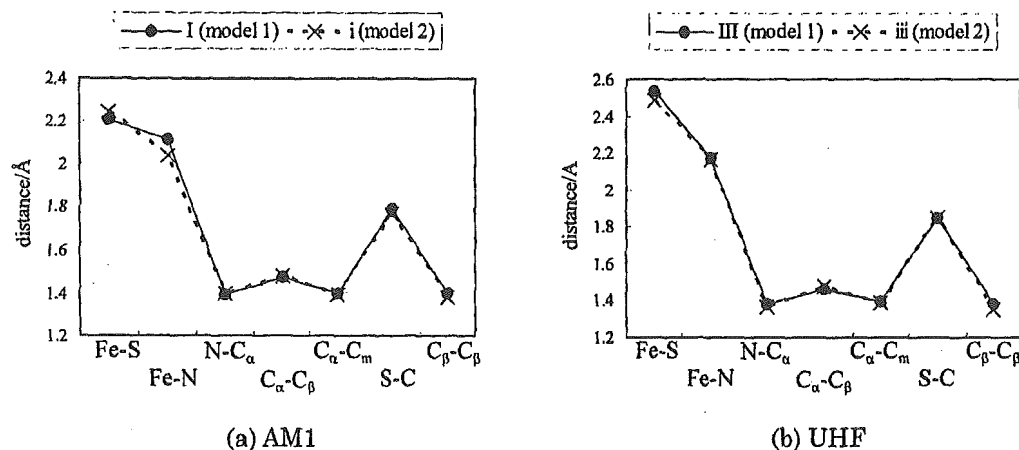


Figure 5. Comparisons of bond lengths in model 1 and 2 optimized by quantum chemical calculations.

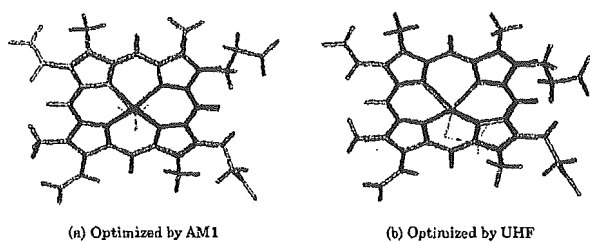


Figure 6. Superposition of model 1 and 2. Model 1 is illustrated in light gray and model 2 in dark gray.

ing, the AM1 method was inadequate for the accurate modeling of P450s, because the N-Fe-N angles and the distance between the  $N_4$  plane and the iron differed from the experimental values. On the other hand, AM1 is a semiempirical method and is therefore not very time-consuming. For example, the computation time for optimizing model 2 was only a few minutes. The results of AM1 calculations were more accurate than those of *ab initio* UHF methods. Therefore, AM1 could be appropriate for rough approximations or the initial calculations of more accurate methods.

The UB3LYP method viii, in which the 6-31G\* basis set was used for iron, produced the same results as UHF. However, the results from method ix, in which the MIDI basis set was used for iron, were in good agreement with experimental structures around the heme iron. In particular, reasonable values for the distance between the  $N_4$  plane and the iron atom, the  $N_{\alpha}$ -Fe- $N_{\alpha}$  angle and the  $N_{\alpha}$ -Fe- $N_{\beta}$  angle, were obtained only with method ix. These results indicate that a UB3LYP method with the MIDI basis set for iron and 4-31G\* for the other elements is the most suited to calculations of P450s. In addition, when comparing methods viii

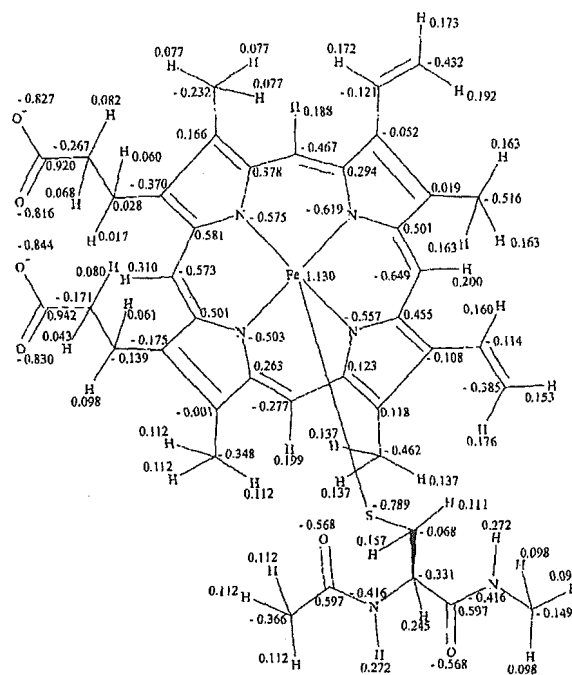


Figure 7. RESP charges calculated for model 1.

and ix, the latter produced more reasonable values for structural features other than those around the iron atom. These results confirm that method ix is applicable when modeling P450s.

The atomic charges for model 1 are illustrated in Figure 7,

Table 3. Optimized Structures for Model 2.

(a) Bond lengths around Fe/Å													
Method	EXAFS 1	EXAFS 2	X-ray 1	X-ray 2	i	ii	iii	iv	v	vi	vii	viii	ix
Fe-S	2.23	2.30	2.20	2.324	2.242	2.489	2.482	2.434	2.464	2.473	2.358	2.441	2.324
Fe-N	2.06	2.05	2.05	2.064	2.038	2.158	2.163	2.193	2.151	2.143	2.171	2.005	2.094

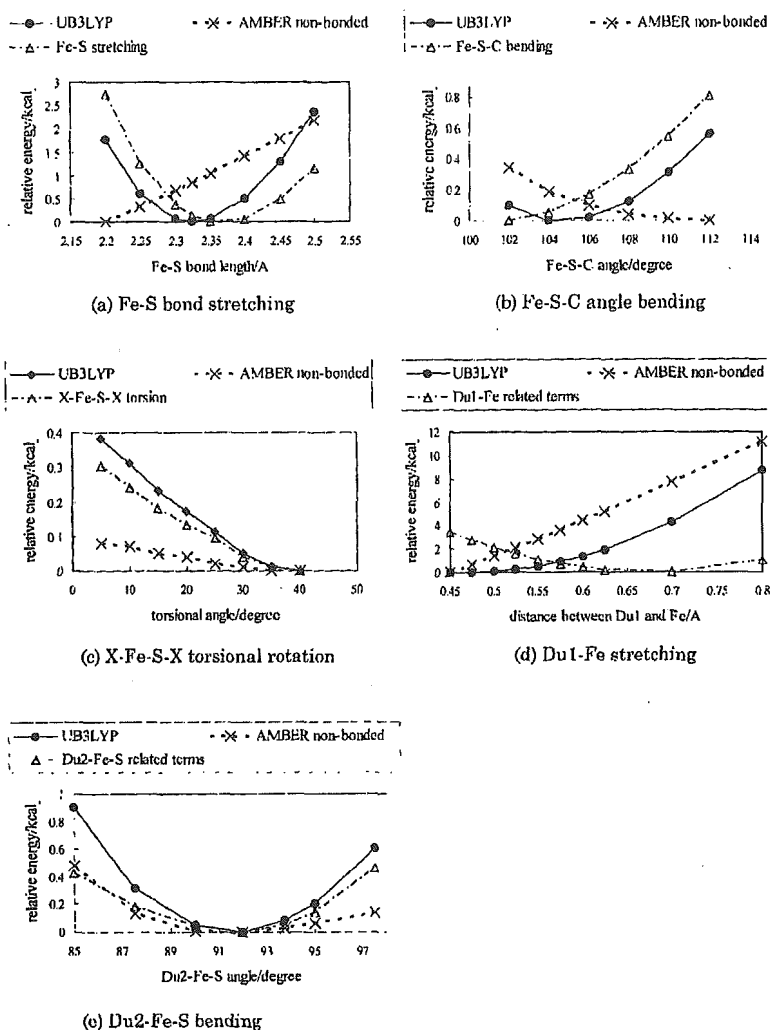
  

(b) Bond angles around Fe/degree													
Method	X-ray 1	X-ray 2	i	ii	iii	iv	v	vi	vii	viii	ix		
$N_{\alpha}$ -Fe- $N_{\alpha}$	155.6	155.7	167.0	145.0	144.7	140.3	148.0	149.7	147.1	168.2	153.7		
$N_{\alpha}$ -Fe- $N_{\beta}$	87.4	87.5	89.3	84.8	84.7	83.4	85.7	86.1	85.7	89.4	87.1		

(c) Distances between $N_4$ plane and Fe/Å													
Method	X-ray 1	X-ray 2	i	ii	iii	iv	v	vi	vii	viii	ix		
$N_4$ -Fe	0.43	0.434	0.231	0.648	0.655	0.744	0.591	0.558	0.588	0.206	0.479		

Optimized structures using various quantum chemical methods for model 2 compared with experimental results.



**Figure 8.** Energy profiles of model 2. The relative value of the energies obtained by UB3LYP (solid line), nonbonded interactions by AMBER force-field (dashed line) and the differences between the solid and the dashed line (alternate long and short dash line) are illustrated.

energy profiles for bond stretching, angle bending, and torsional motion are shown in Figure 8, and the resultant parameters are described in Table 4. The harmonic-oscillator approximations, which play important roles in force fields, cannot be adopted for bond lengths and angles that are far from equilibrium internuclear distances and bond angles. Therefore, energy profiles were obtained between 2.2 and 2.5 Å for Fe-S bond stretching, between 102 and 112° for Fe-S-C angle bending, between 0.45 and 0.80 Å for Du1-Fe stretching, and between 85.0 and 97.5° for Du2-Fe-S bending. The energy profile for X-Fe-S-X torsional motion was calculated between 5 and 40° because of the symmetry of porphyrin. These parameters were calculated to fit the energy differences between the UB3LYP calculations and the nonbonded interactions of the AMBER force field (the alternate long and short dashed

lines in Fig. 8). The values were qualitatively consistent with the atomic charges of other molecules<sup>31</sup> and parameters,<sup>33</sup> and were also quantitatively close to other values. Furthermore, the equilibrium bond length ( $r_{eq}$ ) of Fe-S and the equilibrium bond angle ( $\theta_{eq}$ ) of Fe-S-C were 2.377 Å and 100.8°, respectively, which is consistent with experimental results.

To validate the calculated atomic charges and parameters, MM calculations of P450cam with five-coordinated Fe(III) were carried out. Figure 9 shows that the structures of heme with the axial ligand Cys357 before (dark gray) and after (light gray) the MM calculations were highly similar—the RMSD was only 0.394 Å. This suggests that the force field parameters determined in this study are consistent with the experimental structure of P450cam. Furthermore, the RMSD for porphyrin and Cys357 (excluding the

Table 4. Parameters Calculated by Energy Profiles of Model 2.

(a) Parameters for bond stretching				
	$K_r/\text{kcal} (\text{mol } \text{\AA}^2)^{-1}$	$r_{eq}/\text{\AA}$		
Fe—S	87.589	2.377		
Fe—N	64.594	2.200		
(b) Parameters for angle bending				
	$K_\theta/\text{kcal} (\text{mol } \text{radian}^2)^{-1}$	$\theta_{eq}/\text{degree}$		
Fe—S—C	21.646	100.8		
$N_\alpha$ —Fe— $N_\alpha$	19.683	135.6		
$N_\alpha$ —Fe— $N_\beta$	27.911	88.1		
N—Fe—S	13.277	92.0		
C—N—Fe	47.739	124.3		
(c) Parameters for torsional motion around Fe—S bond				
	No. of paths	$V_n/\text{kcal mol}^{-1}$	$\gamma/\text{degree}$	$n$
X—Fe—S—X	1	0.034	0.0	4.0

side-chain atoms of protoporphyrin IX) was only 0.135 Å. This suggests that the calculated structure around Fe—S is similar to the crystal structure. These results indicate that the RESP charges and the AMBER force field parameters around Fe—S determined in this study are appropriate for use in the modeling of P450s. Further improvements to the MM calculations might be accomplished by refining the parameters around the side-chain atoms of protoporphyrin IX using quantum chemical calculations.

Additional validation of these atomic charges and force-field parameters has already been reported.<sup>42</sup> In ref. 42, homology models of the wild types and mutants of human CYP2C19 and CYP2C9 were constructed, and the structures of these 11 proteins were refined by MM and CMD calculations using the parameters determined in this study. The results of computational docking studies on these models with (S)-mephenytoin, which is one of the specific substrates of CYP2C19, reproduced the experimental enzyme activities without exception. Furthermore, in the calculated three-dimensional structure of the CYP2C19-(S)-mephenytoin complex, the 4'-hydrogen of (S)-mephenytoin was close to the heme iron, which was consistent with the experimentally observed 4'-hydroxylation activity of (S)-mephenytoin. These results suggest that the force field parameters determined in this study, which play significant roles in the construction of models, are reasonable for use in calculations on P450s. Therefore, quantum chemical calculations on model 2 using the UB3LYP method, with the MIDI basis set for iron and the 4-31G\* basis set for other elements, appear to be suitable for preparing force field parameters for MM and CMD.

In this study, classical force field parameters of P450s were determined. Although they are useful tools for calculations of

biopolymers, ligand-protein interactions are represented by only van der Waals and Coulombic terms. Static structures of ligand-protein complexes, especially inhibitor-protein complexes, can be predicted and refined in reasonable costs by using classical force field. However, for more detailed analyses of ligand-protein interactions such as enzymatic reaction, which is interesting and important in the dynamic properties of substrate-protein complexes, classical mechanical methods are inadequate because electronic state changes induced by ligand docking play significant roles in these systems. To these purposes, quantum chemical treatment of complexes, for example, QM/MM method or all-electron calculations, are indispensable.

## Conclusions

Simplified models are useful if a number of quantum chemical calculations are required on large systems, such as P450s. In this study, an Fe(III) porphyrin with a methylthio group as its axial ligand was used in place of Fe(III) protoporphyrin IX, the axial ligand of which is ACE-CYS-NME. Comparing the results of quantum calculations using various methods suggests that MIDI with Hay's diffuse basis sets are preferable for iron, and that the UB3LYP method is appropriate for high-spin state iron-porphyrin systems with five-coordinated Fe(III). Although the semiempirical AM1 method gave the second-best results after DFT, the structure around the iron atom differed between models 1 and 2. These results might indicate that additional AM1-d parameters for iron do not always work well because the original AM1 method does not include parameters for transition metals. As the AM1 method is highly time-effective, more detailed studies of its strengths and weaknesses are required. We intend to investigate these factors further in a future study.

By using the series of quantum chemical calculations described in this study, atomic charges and force field parameters, which are essential tools of MM and CMD simulations, can be prepared for the study of proteins that include a nonamino acidic molecule. Computer-aided drug design trials, such as *de novo* design and virtual screening, could be carried out for a wide variety of drug targets using these calculations.

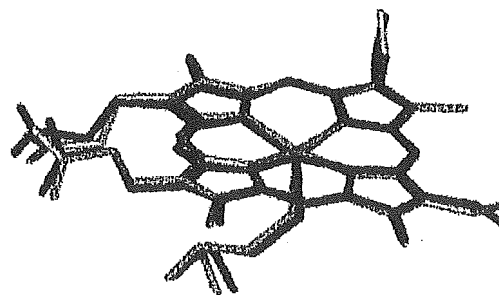


Figure 9. Comparison of the structure of heme and Cys357 before and after minimization (dark and light gray, respectively) using the AMBER force-field with obtained parameters.

## References

1. Miller, W. L. *Endocr Rev* 1988, 9, 295.
2. Capdevila, J.; Chacos, N.; Werringloer, J.; Prough, R. A.; Estabrook, R. W. *Proc Natl Acad Sci USA* 1981, 78, 5362.
3. Makita, K.; Falck, J. R.; Capdevila, J. H. *FASEB J* 1996, 10, 1456.
4. Leo, M. A.; Iida, S.; Lieber, C. S. *Arch Biochem Biophys* 1984, 234, 305.
5. Leo, M. A.; Lasker, J. M.; Raucy, J. L.; Cho-il, K.; Black, M.; Lieber, C. M. *Arch Biochem Biophys* 1989, 269, 305.
6. Wrighton, S. A.; Stevens, J. C. *Crit Rev Toxicol* 1992, 22, 1.
7. Guengerich, F. P. *J Pharmacokinet Biopharm* 1996, 24, 521.
8. Ingelman-Sundberg, M. *Trends Pharmacol Sci* 2004, 25, 193.
9. Schlichting, I.; Berendzen, J.; Chu, K.; Stock, A. M.; Maves, S. A.; Benson, D. E.; Sweet, R. M.; Ringe, D.; Petsko, G. A.; Sligar, S. G. *Science* 2000, 287, 1615.
10. Fisher, M. T.; Sligar, S. G. *J Am Chem Soc* 1985, 107, 5018.
11. Harris, D.; Loew, G.; Waskell, L. *J Am Chem Soc* 1998, 120, 4308.
12. Harris, D. L.; Loew, G. H. *J Am Chem Soc* 1998, 120, 8941.
13. Ogliaro, F.; de Visser, S. P.; Cohen, S.; Kaneti, J.; Shaik, S. *Chem BioChem* 2001, 11, 848.
14. Ogliaro, F.; Filatov, M.; Shaik, S. *Eur J Inorg Chem* 2000, 2455.
15. de Visser, S. P.; Ogliaro, F.; Harris, N.; Shaik, S. *J Am Chem Soc* 2001, 123, 3037.
16. Scherlis, D. A.; Cymeryng, C. B.; Estrin, D. A. *Inorg Chem* 2000, 39, 2352.
17. de Visser, S. P.; Ogliaro, F.; Sharma, P. K.; Shaik, S. *J Am Chem Soc* 2002, 124, 11809.
18. de Visser, S. P.; Kumar, D.; Cohen, S.; Shacham, R.; Shaik, S. *J Am Chem Soc* 2004, 126, 8362.
19. de Groot, M. J.; Havenith, R. W. A.; Vinkers, H. M.; Zwaans, R.; Vermeulen, N. P. E.; van Lenthe, J. H. *J Comput-Aided Mol Des* 1998, 12, 183.
20. Filatov, M.; Harris, N.; Shaik, S. *J Chem Soc, Perkin Trans 2* 1999, 399.
21. Nakano, T.; Kaminuma, T.; Sato, T.; Akiyama, Y.; Uebayasi, M.; Kitaura, K. *Chem Phys Lett* 2000, 318, 614.
22. Sato, F.; Shigemitsu, Y.; Okazaki, I.; Yahiro, S.; Fukue, M.; Kozuru, S.; Kashiwagi, H. *Int J Quant Chem* 1997, 63, 245.
23. Guallar, V.; Fricnsner, R. A. *J Am Chem Soc* 2004, 126, 8501.
24. Autenrieth, F.; Tajkhorshid, E.; Baudry, J.; Luthey-Schulten, Z. *J Comp Chem* 2004, 25, 1613.
25. Tatewaki, H.; Huzinaga, S. *J Chem Phys* 1980, 72, 339.
26. Hay, P. J. *J Chem Phys* 1977, 66, 4377.
27. Mulliken, R. S. *J Chem Phys* 1955, 23, 1833.
28. Breneman, C. M.; Wiberg, K. B. *J Comp Chem* 1990, 11, 361.
29. Singh, U. C.; Kollman, P. A. *J Comp Chem* 1984, 5, 129.
30. Bayly, C. I.; Cieplak, P.; Cornell, W. D.; Kollman, P. A. *J Phys Chem* 1993, 97, 10269.
31. Cieplak, P.; Cornell, W. D.; Bayly, C.; Kollman, P. A. *J Comp Chem* 1995, 16, 1357.
32. Case, D. A.; Pearlman, D. A.; Caldwell, J. W.; Cheatham, T. E., III; Ross, W. S.; Simmerling, C. L.; Darden, T. A.; Merz, K. M.; Stanton, R. V.; Cheng, A. L.; Vincent, J. J.; Crowley, M.; Tsui, V.; Radmer, R. J.; Duan, Y.; Pitera, J.; Massova, I.; Seibel, G. L.; Singh, U. C.; Weiner, P. K.; Kollman, P. A. *AMBER 6*; University of California: San Francisco, 1999.
33. Cornell, W. D.; Cieplak, P.; Bayly, C. I.; Gould, I. R.; Merz, K. M.; Ferguson, D. M.; Spellmeyer, D. C.; Fox, T.; Caldwell, J. W.; Kollman, P. A. *J Am Chem Soc* 1995, 117, 5179.
34. Poulos, T. L.; Finzel, B. C.; Howard, A. J. *J Mol Biol* 1987, 195, 687.
35. SYBYL 6.9.2; Tripos Inc.; St. Louis, 2004.
36. Stewart, J. J. P. *MOPAC2002*; Fujitsu Limited: Tokyo, 2001.
37. Frisch, M. J.; Trucks, G. W.; Schlegel, H. B.; Scuseria, G. E.; Robb, M. A.; Cheeseman, J. R.; Zakrzewski, V. G.; Montgomery, J. A.; Stratmann, R. E.; Burant, J. C.; Dapprich, S.; Millam, J. M.; Daniels, A. D.; Kudlin, K. N.; Strain, M. C.; Farkas, O.; Tomasi, J.; Barone, V.; Cossi, M.; Cammi, R.; Mennucci, B.; Pomelli, C.; Adamo, C.; Clifford, S.; Ochterski, J.; Petersson, G. A.; Ayala, P. Y.; Cui, Q.; Morokuma, K.; Malick, D. K.; Rabuck, A. D.; Raghavachari, K.; Foresman, J. B.; Cioslowski, J.; Ortiz, J. V.; Baboul, A. G.; Stefanov, B. B.; Liu, G.; Liashenko, A.; Piskorz, P.; Komaromi, I.; Gomperts, R.; Martin, R. L.; Fox, D. J.; Keith, T.; Al-Laham, M. A.; Pong, C. Y.; Nanayakkara, A.; Gonzalez, C.; Challacombe, M.; Gill, P. M. W.; Johnson, B. G.; Chen, W.; Wong, M. W.; Andres, J. L.; Head-Gordon, M.; Replogle, E. S.; Pople, J. A. *Gaussian 98 Revision A.7*; Gaussian, Inc.: Wallingford, 1998.
38. Hahn, J. E.; Hodgson, K. O. *J Biol Chem* 1982, 257, 10934.
39. Cramer, S. P.; Dawson, J. H.; Hodgson, K. O.; Hager, L. P. *J Am Chem Soc* 1978, 100, 7282.
40. Tang, S. C.; Koch, S.; Papaefthymiou, G. C.; Foner, S.; Frankel, R. B.; Ibers, J. A.; Holm, R. H. *J Am Chem Soc* 1976, 98, 2414.
41. Choithia, C.; Lesk, A. M. *EMBO J* 1986, 5, 823.
42. Oda, A.; Yamaotsu, N.; Hirono S. *Pharm Res* 2004, 21, 2270.

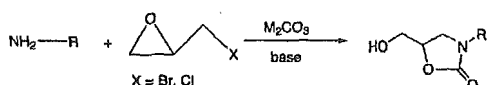
## Convenient Synthesis of Oxazolidinones by the Use of Halomethyloxirane, Primary Amine, and Carbonate Salt

Yumiko Osa, Yuka Hikima, Yoko Sato, Kouichi Takino, Yoshihiro Ida, Shuichi Hirono, and Hiroshi Nagase\*

School of Pharmaceutical Sciences, Kitasato University, 5-9-1, Shirokane, Minato-ku, Tokyo 108-8641, Japan

nagaseh@pharm.kitasato-u.ac.jp

Received January 26, 2005



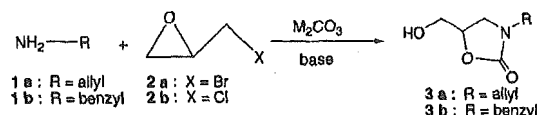
Primary amines reacted with carbonate salts ( $\text{Na}_2\text{CO}_3$ ,  $\text{K}_2\text{CO}_3$ ,  $\text{Cs}_2\text{CO}_3$ , and  $\text{Ag}_2\text{CO}_3$ ) and halomethyloxiranes in the presence of a base such as DBU or TEA to give oxazolidinones in high yields. The use of  $\text{K}_2\text{CO}_3$  among these carbonate gave the best yield in this synthesis. A reaction mechanism was proposed that the oxazolidinone was obtained from an oxazinanone intermediate via a bicyclo[2.2.1] intermediate. The present reaction can be widely applied to convenient synthesis of useful N-substituted oxazolidinones and chiral oxazolidinones.

Oxazolidinones can be used as the precursors of naturally occurring amino alcohols and amino acids which have been synthesized by a variety of methods.<sup>1</sup> In addition, they are useful as chiral auxiliaries<sup>2</sup> in asymmetric synthesis.<sup>1a</sup> Recently, some oxazolidinone derivatives such as DUP-105,<sup>3</sup> DUP-721,<sup>3</sup> and linezolid (Zyvox)<sup>3b,4</sup> have attracted much interest as monodrug- or multidrug-resistant antibacterial agents.<sup>5</sup> Early synthesis of oxazolidinones was carried out via the reactions of 1,2-amino alcohols and phosgene or its derivatives<sup>6</sup> or amino alcohols with carbon dioxide under high pressure.<sup>7</sup> Recently, carbohydrate derivatives were also used in the synthesis of oxazinanone and oxazolidinone.<sup>8</sup> However, these methods required multiple steps, and the total

\* To whom correspondence should be addressed. Tel: +81-3-5791-6372. Fax: +81-3-4442-5707.

- (1) (a) Ager, D. J.; Prakash, I.; Schaad, D. R. *Chem. Rev.* 1998, 96, 835–876. (b) Dyen, M. E.; Swern, D. *Chem. Rev.* 1967, 67, 197–246.
- (2) (a) Evans, D. A.; Bartroli, J.; Shih, T. L. *J. Am. Chem. Soc.* 1981, 103, 2127–2129. (b) Evans, D. A. *Aldrichim. Acta* 1982, 15, 23–32. (c) Evans, D. A.; Takacs, J. M.; McGee, L. R.; Ernis, M. D.; Mathre, D. J.; Bartroli, J. *Pure Appl. Chem.* 1981, 53, 1109–1127.
- (3) (a) Gregory, W. A.; Brittelli, D. R.; Wang, C.-L. J.; Wuonola, M. A.; McRipley, R. J.; Eustice, D. C.; Eberly, V. S.; Bartholomew, P. T.; Slee, A. M.; Forbes, M. *J. Med. Chem.* 1989, 32, 1673–1681. (b) Gordeev, M. F. *Curr. Opin. Drug Discovery Devel.* 2001, 4, 450–461. (c) Slee, A. M.; Wuonola, M. A.; McRipley, R. J.; Zajac, I.; Zawada, M. J.; Bartholomew, P. T.; Gregory, W. A.; Forbes, M. *Antimicrob. Agents Chemother.* 1987, 31, 1791–1797.
- (4) (a) Bolmstrom, A.; Ballow, C. H.; Qvarnstrom, A.; Biedebach, D. J.; Jones, R. N. *Clin. Microbiol. Infect.* 2002, 8, 791–800. (b) Barbachyn, M. R.; Ford, C. W. *Angew. Chem., Int. Ed.* 2003, 42, 2010–2023. (c) Wang, G.; Hollingsworth, R. I. *Tetrahedron: Asymmetry* 2000, 11, 4429–4432.
- (5) Barbachyn, M. R.; Toops, D. S.; Grega, K. C.; Hendges, S. K.; Ford, C. W.; Zurenko, G. E.; Hamel, J. C.; Shaadt, R. D.; Stapert, D.; Yagi, B. H.; Buyses, J. M.; Demyan, W. F.; Kilburn, J. O.; Glickman, S. E. *Bioorg. Med. Chem. Lett.* 1996, 6, 1009–1014.

### SCHEME 1



yields were not always high. As an improved method to overcome the defects, cyclic carbamate synthesis by use of carbon dioxide dissolved in protic solvents containing amines and oxiranes was reported by Toda et al.<sup>9</sup> When primary amines reacted with halomethyloxiranes and a large amount of carbon dioxide under neutral conditions, six-membered cyclic carbamates of oxazinanones were formed.<sup>10</sup> They proposed a reaction mechanism by which the ammonium carbamate intermediate reacted with oxirane. They also used 2-(1-haloalkyl)oxirane and primary amine in the presence of cesium carbonate ( $\text{Cs}_2\text{CO}_3$ ) and proposed a mechanism by which carbon dioxide derived from  $\text{Cs}_2\text{CO}_3$  reacted with the intermediate (2-alkyl-3-aminomethyloxirane) to form oxazolidinone.<sup>11</sup> However, these reactions did not give a high yield of oxazolidinone.

We have recently found a simple method to synthesize oxazolidinone derivatives using primary amine and halomethyloxirane in the presence of various carbonate salts. The reaction is shown in Scheme 1.

At the beginning of our research, we used allylamine (1a, 2 molar equiv), which reacted with halomethyloxirane (2, 2 molar equiv, bromomethyloxirane 2a, and chloromethyloxirane 2b) in the presence of potassium carbonate or silver carbonate (1 molar equiv) in methanol at room temperature to afford oxazolidinone in 45% yield. The structure of *N*-allyl-5-hydroxymethyloxazolidin-2-one

- (6) (a) Newman, M. S.; Kutner, A. J. *J. Am. Chem. Soc.* 1951, 73, 4199–4204. (b) Lubell, W.; Rappoport, H. *J. Org. Chem.* 1989, 54, 3824–3831. (c) Bonner, M. P.; Thornton, E. R. *J. Am. Chem. Soc.* 1991, 113, 1299–1308. (d) Palomo, C.; Berree, F.; Lindert, A.; Villalgorido, J. M. *J. Chem. Soc., Chem. Commun.* 1994, 1861–1862. (e) Efskind, J.; Romming, C.; Undheim, K. *J. Chem. Soc., Perkin Trans. 1* 1999, 1677–1684.

- (7) (a) Lynn, J. W. U. S. Patent 2,975,187, 1961; *Chem. Abstr.* 1961, 55, 16568. (b) Steele, A. B. U. S. Patent 2,868,801, 1959; *Chem. Abstr.* 1959, 53, 10261.

- (8) (a) Hu, N. X.; Aso, Y.; Otsubo, T.; Ogura, F. *J. Chem. Soc., Chem. Commun.* 1987, 1447–1448. (b) Lewis, N.; McKillop, A.; Taylor, R. J. K.; Watson, R. J. *Synth. Commun.* 1995, 25, 561–568. (c) Li, G.; Lenington, S.; Willis, S.; Kim, S. H. *J. Chem. Soc., Perkin Trans. 1* 1998, 1753–1764. (d) Ferozi, M.; Inesi, A.; Mucciante, V.; Rossi, L. *Tetrahedron Lett.* 1999, 40, 6059–6060. (e) Tanimori, S.; Kirihata, M. *Tetrahedron Lett.* 2000, 41, 6785–6788. (f) Casadei, M. A.; Ferozi, M.; Inesi, A.; Rossi, L.; Sotgiu, G. *J. Org. Chem.* 2000, 65, 4759–4761. (g) Caggiano, L.; Davies, J.; Fox, D. J.; Moody, D. C.; Warren, S. *Chem. Commun.* 2003, 1650–1651. (h) Dinsmore, C. J.; Mercer, S. P. *Org. Lett.* 2004, 6, 2885–2888. (i) Ella-Menye, J.-R.; Sharma, V.; Wang, G. *J. Org. Chem.* 2005, 70, 463–469.

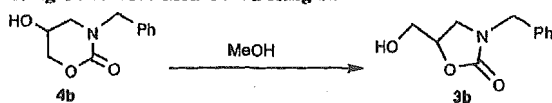
- (9) (a) Toda, T. *Chem. Lett.* 1977, 957–958. (b) Saito, N.; Hatakeda, K.; Ito, S.; Asano, T.; Toda, T. *Heterocycles* 1981, 15, 905–906. (c) Toda, T. *Nippon Kagaku Kaishi* 1982, 2, 282–288. (d) Saito, N.; Hatakeda, K.; Ito, S.; Asano, T.; Toda, T. *Bull. Chem. Soc. Jpn.* 1986, 59, 1629–1631. (e) Toda, T.; Kitagawa, Y. *Angew. Chem., Int. Ed. Engl.* 1987, 26, 334–335. (f) Saito, N.; Hatakeda, K.; Ito, S.; Asano, T.; Namai, Y.; Toda, T. *Agric. Biol. Chem.* 1987, 51, 1193–1194.

- (10) (a) Asano, T.; Saito, N.; Ito, S.; Hatakeda, K.; Toda, T. *Chem. Lett.* 1978, 311–312. (b) Saito, N.; Hatakeda, K.; Ito, S.; Asano, T.; Toda, T. *Nippon Kagaku Kaishi* 1986, 9, 1196–1201.

- (11) Yoshida, M.; Ohshima, M.; Toda, T. *Heterocycles* 1993, 35, 623–626.



TABLE 1. Conversion Conditions of Six-Membered Ring 4b to Five-Membered Ring 3b



run <sup>a</sup>	molar ratio		reaction	yield (%)	
	4b/1b <sup>b</sup>	base (equiv)		3b	recovery 4b
1	1:0:0		reflux, o.n. <sup>c</sup>		100
2	2:2:1:0		rt, stirring, o.n.	94	
3	2:2:1:0		reflux, 2 hr	quant	
4	1:0:0:5	DBU	reflux, 5.5 hr	96	
5	1:0:0:5	TEA	reflux, o.n.		100
6	1:0:0:4	TEA (3), DBU (1)	reflux, o.n.	quant.	

<sup>a</sup> All reactions were carried out in MeOH. <sup>b</sup> 1b = NH<sub>2</sub>CH<sub>2</sub>-Ph. <sup>c</sup> o.n. = overnight.

(3a) obtained from allylamine (1a) was determined, in detail, using <sup>1</sup>H NMR, <sup>13</sup>C NMR, <sup>1</sup>H-<sup>1</sup>H decoupling, NOE, and LSPD<sup>12</sup> and also was supported by X-ray analysis.<sup>13</sup> Furthermore, it was confirmed that the carbon of the carbonate salt was introduced at the 2-position in 3a by the reaction using isotopic Ag<sub>2</sub><sup>13</sup>CO<sub>3</sub> (98% atomic purity of <sup>13</sup>C) instead of K<sub>2</sub>CO<sub>3</sub>.

To elucidate the reaction mechanism and increase the yields, the IR spectrum of the reaction mixture, which was obtained by the reaction of molar ratios of K<sub>2</sub>CO<sub>3</sub> (1 mol), benzylamine (instead of allylamine because of its high boiling point compared with that of allylamine), and bromomethyloxirane (2 mol) in methanol at 0 °C, was measured. We found the bands at 1680 and 1730 cm<sup>-1</sup> in the reaction mixture. The former band is assigned<sup>14</sup> to a six-membered cyclic carbamate of oxazinanone, which was also reported by Toda et al.<sup>9c</sup> The latter band corresponds to a five-membered cyclic carbamate of oxazolidinone. The spot of oxazinanone in TLC (the value of R<sub>f</sub> was 0.47; chloroform/methanol = 10:1) diminished with the reaction time. On the other hand, the spot of oxazolidinone in TLC (the value of R<sub>f</sub> was 0.58; chloroform/methanol = 10:1) enlarged with the reaction time. These facts support that oxazinanone is an unstable intermediate (kinetic product) in the reaction.

For further confirmation of oxazinanone formation in the reaction process, the isomerization of *N*-benzyl-5-hydroxyoxazinanone (4b) to *N*-benzyl-5-hydroxymethyl-oxazolidinone (3b) was examined as shown in Table 1. When only 4b was refluxed in methanol, 3b was not obtained and 4b was recovered (run 1). On the other hand, the reaction conditions (even if at room temperature) for oxazolidinone synthesis in the presence of K<sub>2</sub>CO<sub>3</sub> gave 3b in 94% yield (run 2). These facts showed that K<sub>2</sub>CO<sub>3</sub> is necessary for the conversion of 4b to 3b. Furthermore, under reflux for 2 h, 3b was obtained quantitatively (run 3). The use of DBU instead of K<sub>2</sub>CO<sub>3</sub>

also gave 3b in 96% yield (run 4), but by the use of TEA instead of K<sub>2</sub>CO<sub>3</sub> 4b was quantitatively recovered (run 5). When 1 equiv of DBU was added after addition of 3 equiv of TEA to the reaction solution, 3b was obtained in quantitative yield (run 6). The above results showed that the ring contraction reaction from six-membered cyclic carbamate to five-membered cyclic carbamate perfectly proceeded in the presence of K<sub>2</sub>CO<sub>3</sub> or DBU but did not occur in the presence of only TEA. These results mean that a strong base or a basic condition is necessary to form 3b.

Furthermore, total molecular energy calculation of compounds 3b and 4b was carried out by the use of Merck Molecular Force Field (MMFF94).<sup>15</sup> The total energy of 3b is 31.2 kcal/mol and that of 4b is 34.1 kcal/mol. Therefore, the calculation result shows that oxazolidinone is more stable than oxazinanone. This result also supports that the six-membered ring is an intermediate of the reaction process. Wang et al. also reported six-membered ring oxazinanone was converted to more stable five-membered ring oxazolidinone under base conditions and heating,<sup>9i</sup> which gave supporting evidence in our present conversion.

Based on the above discussion, a reaction mechanism is proposed as depicted in Scheme 2. Two routes (I and II) are supposed to form an intermediate D. In route I, first, primary amine 1 attacks the C-X bond of halomethyloxirane 2 to afford an intermediate A. Subsequently, a carbonate ion attacks A to form the intermediate D. In route II, 1 attaches the oxirane ring of 2 to give intermediate B. As oxirane ring 2 may be more electrophilic than the C-X bond in the case of an attack of the alkoxide ion,<sup>16</sup> a first attack of amine 1 to the oxirane ring may be reasonably considered.<sup>16,17</sup> Subsequently, the resulting alkoxide ion of intermediate B attacks the carbon atom of the halomethyl group to form C. Next, the carbonate ion attacks the oxirane ring C to afford the intermediate D. Then the resulting amino nitrogen attacks the carbonyl group in D to cyclize intramolecularly to a six-membered ring of oxazinanone (4). In the mechanism, the intermediate D can cyclize only to six-membered oxazinanone, not five-membered oxazolidinone. Two routes III and IV are considered as the conversion process of oxazolidinone (3) from compound 4. In route III, the alkoxide ion in intermediate E under strong basic condition attacks intramolecularly the carbonyl carbon to give a bicyclo[2.2.1] intermediate F, which is subsequently converted to a five-membered ring of oxazolidinone 3. In route IV, a methoxide ion generated from methanol under strong basic condition attacks the carbonyl carbon of the oxazinanone (intermediate G) to open a ring structure. The resulting alkoxide ion (intramolecularly) attacks the carbon of intermediate H to form compound 3. However, it is considered that the intramolecular attack in route III may be more favorable (entropic) than the intermolecular one of the methoxide

(12) (a) Takeuchi, S.; Uzuwa, J.; Seto, H.; Yonehara, H. *Tetrahedron Lett.* 1977, 32, 2943-2946. (b) Seto, H.; Sasaki, T.; Yonehara, H.; Uzuwa, J. *Tetrahedron Lett.* 1978, 10, 923-926. (c) LSPD (long range selective proton decouple) was used to detect the ring protons adjacent to the oxygen and nitrogen atoms linked to carbonyl carbon.

(13) Osa, Y.; Sato, Y.; Hatano, A.; Takeda, K.; Takino, K.; Takayanagi, H. *Anal. Sci.* 2003, 19, x17-x18.

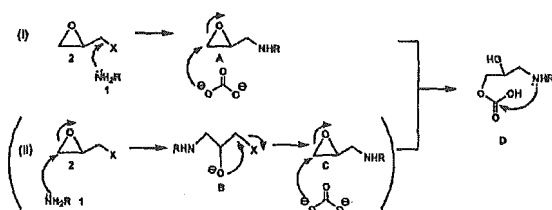
(14) *The Aldrich Library of FT-IR Spectra*, Edition II; Aldrich: Milwaukee, 1997.

(15) (a) Halgren, T. A. *J. Am. Chem. Soc.* 1992, 114, 7827-7843. (b) Halgren, T. A. *J. Comput. Chem.* 1996, 17, 490-519.

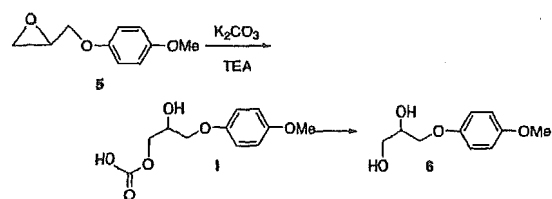
(16) Clayden, J.; Greeves, N.; Warren, S.; Wothers, P. *Organic Chemistry*; Oxford University Press: Oxford, 2001.

(17) The textbook of organic chemistry (for example, the book written by Warren<sup>15</sup>) described the oxirane ring of epichlorohydrin is more electrophilic than the C-Cl bond with alkoxide. Therefore, the carbonate ion was reacted with the oxirane ring of epibromohydrin.

SCHEME 2



SCHEME 3



ion in route IV. Therefore, we think route III may be more reasonable. Compound 4 will be formed as a kinetic product and 3 can be obtained as a thermodynamic product.

The difference between our mechanism and that of Toda was mainly the reaction intermediate. In the Toda mechanism,<sup>11</sup> the carbamate anion was formed by reacting 2-(1-haloalkyl)oxirane and amine with CO<sub>2</sub> derived from Cs<sub>2</sub>CO<sub>3</sub> to open the epoxide in the alkaline medium and the resulting alkoxide ion attacks at the C-X carbon to give an epoxy ring. However, as carbonate (Cs<sub>2</sub>CO<sub>3</sub>) could not be converted to CO<sub>2</sub> under the strong basic condition using CsOH, CO<sub>2</sub> could not be produced to form the carbamate ion. In our mechanism, the carbonate ion, not the carbamate anion, attacks the halomethyloxirane directly.

Furthermore, the reactivity (nucleophilicity) of the carbonate ion was confirmed by the reaction of 2,3-epoxypropyl 4-methoxyphenyl ether (5) and K<sub>2</sub>CO<sub>3</sub>. Though the reaction of 5 and K<sub>2</sub>CO<sub>3</sub> (dried in vacuo at 120 °C for 10 h) in anhydrous DMF gave no products under the anhydrous condition, the addition of TEA to the solution containing 5 and K<sub>2</sub>CO<sub>3</sub> in anhydrous DMF under anhydrous condition afforded a diol (6) which was obtained by hydrolysis of the carbonate intermediate I in 43% yield<sup>18</sup> (Scheme 3). The preparation of the product, diol (6), suggests attack of the carbonate ion to oxirane in the presence of a base.

On the basis of the above proposed reaction mechanism as shown in Scheme 2, we examined optimization of the reaction conditions. In Scheme 2, the excess of reagents for primary amine was expected to increase the yields, and strong basic condition would be needed for formation for the alkoxide ion to attack the carbonyl carbon (E, F) and reflux condition would be able to convert the six-membered ring, oxazinanone, to the five-membered ring, oxazolidinone, easily. Table 2 shows various conditions to optimize various molar ratios of the reagents and temperature. The high yield of *N*-benzyl-5-hydroxy-

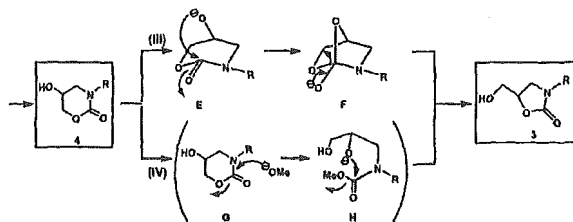


TABLE 2. Reaction Conditions for Synthesis of 3b

1b		2a, X=Br 2b, X=Cl		K <sub>2</sub> CO <sub>3</sub> /TEA		MeOH		HO-CH <sub>2</sub> -CH <sub>2</sub> -N(CH <sub>2</sub> Ph) <sub>2</sub>	
run	X	molar ratio 1b/2/K <sub>2</sub> CO <sub>3</sub> /TEA		reaction	yield of 3b (%)				
1	Br	1:1:1:1	rt, o.n. <sup>a</sup>	28					
2	Br	1:1:1:1	reflux, o.n.	37					
3	Br	1:2:2:2	rt, o.n.	29					
4	Br	1:3:1:1	rt, o.n.	61					
5	Br	1:5:5:5	rt, o.n.	68					
6	Br	1:5:5:0	reflux, o.n.	76					
7	Br	1:5:5:5	reflux, o.n.	83					
8	Br	1:10:10:10	rt, o.n.	58					
9	Br	1:10:10:10	reflux, o.n.	88					
10	Cl	1:5:5:5	reflux, o.n.	81					

<sup>a</sup> o.n. = overnight.

methyloxazolidin-2-one (3b) (more than 80% yield) was obtained under the conditions of a large mole ratio (more than 5 molar equiv) of halomethyloxirane, K<sub>2</sub>CO<sub>3</sub> in methanol in the presence of more than 5 mol base (TEA; triethylamine or DBU; 1,8-diazabicyclo[5.4.0]undec-7-ene) per mole of amine under reflux (runs 7, 9, and 10).

The use of one molar ratio of 1b, 1 or 2 molar ratio of 2b, K<sub>2</sub>CO<sub>3</sub>, and TEA gave a low yield of 3b (runs 1 and 3), and the yield of 3b did not increase even under reflux (37%, run 2). Excess amounts (5 or 10 molar ratios) of 2a, K<sub>2</sub>CO<sub>3</sub>, and TEA to benzylamine 1b at room temperature gave 3b in 68% and 58% yields (runs 5 and 8) and the yields increased to 83 and 88% under reflux (runs 7 and 9). In the absence of TEA as a base, the yield of 3b was lower than that in run 7 (run 6). It suggested that the addition of a strong base increased the yield of 3b in comparison between runs 6 and 7. The use of chloromethyloxirane 2b instead of bromomethyloxirane 2a gave almost the same yield of 3b (81% yields in the case of 2b (run 10) and 83% in the case of 2a (run 7)). Thus, we were able to optimize the reaction conditions for oxazolidinones on the basis of our reaction mechanism. Pure product 3 was rationally identified on the basis of IR, NMR, elemental analysis, and mass spectra.

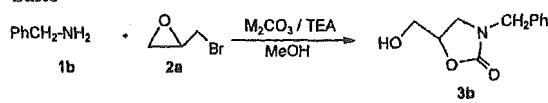
Several kinds of carbonate salts were examined to obtain 3 as shown in Table 3. Na<sub>2</sub>CO<sub>3</sub>, Cs<sub>2</sub>CO<sub>3</sub>, and Ag<sub>2</sub>CO<sub>3</sub> (runs 2, 4, and 6) gave more than 75% yields of 3b.

At the beginning of our study,<sup>19</sup> we examined various primary amines of propyl, isopropyl, *n*-butyl, heptyl, and cyclohexyl groups. When the reaction conditions of pri-

(18) Tanzer, W.; Muller, H.; Wintzer, J.; Fedtke, M. *Makromol. Chem.* 1987, 188, 2857-2863.

(19) Osa, Y.; Sato, Y.; Oshimoto, M.; Takino, K.; Takeda, A.; Takayanagi, H. 44th Symposium of J. Synth. Org. Chem., Jpn. Kanto Branch, Niigata, 2002, Abstract pp 123-124.

TABLE 3. The Yield of 3b Using Various Carbonate Salts



run <sup>a</sup>	molar ratio		reaction	yield of 3b (%)
	M <sub>2</sub> CO <sub>3</sub>	1b/2a/ M <sub>2</sub> CO <sub>3</sub> /TEA		
1	K <sub>2</sub> CO <sub>3</sub>	1:5:5:5	reflux, under Ar, o.n. <sup>b</sup>	83
2	Na <sub>2</sub> CO <sub>3</sub>	1:5:5:5	reflux, under Ar, o.n.	77
3	Rb <sub>2</sub> CO <sub>3</sub>	1:5:5:5	reflux, under Ar, o.n.	28
4	Cs <sub>2</sub> CO <sub>3</sub>	1:5:5:5	reflux, under Ar, o.n.	82
5	Li <sub>2</sub> CO <sub>3</sub>	1:5:5:5	reflux, under Ar, o.n.	25
6	Ag <sub>2</sub> CO <sub>3</sub>	1:5:5:5	reflux, dark, under Ar, o.n.	75

<sup>a</sup> All reactions were carried out in MeOH. <sup>b</sup> o.n. = overnight.

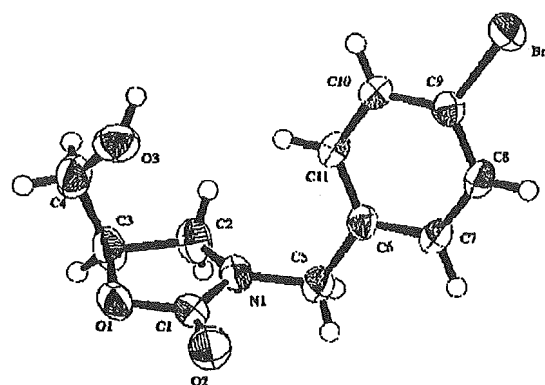
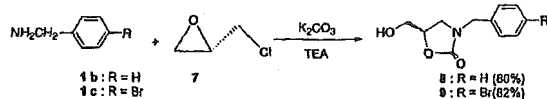


FIGURE 1.

SCHEME 4



mary amine 1 (2 equiv), bromomethyloxirane 2a (2 equiv), and Ag<sub>2</sub>CO<sub>3</sub> or K<sub>2</sub>CO<sub>3</sub> (1 equiv) in methanol stirring overnight at room temperature were used, 36–50% yields of the corresponding oxazolidinones were obtained based on each amine. Application of similar optimum reaction conditions to benzylamine will give higher yield of oxazolidinones. The use of aniline as aromatic amine is now under study.

We also applied chiral halomethyloxirane to a synthesis for chiral oxazolidinones to confirm which route the reaction selected, I or II. The reactions of (*S*)-chloromethyloxirane (7) with benzylamine (1b) and *p*-bromobenzylamine (1c) under similar conditions to the above method to give oxazolidinones 8 and 9 were carried out (Scheme 4). The stereo structure of *N*-(*p*-bromobenzyl)-5-hydroxymethyloxazolidin-2-one (9) was confirmed by means of X-ray analysis (Figure 1).<sup>20</sup> In this reaction, the *S*-configuration of the oxirane ring inverted to the *R*-configuration at the 5-position of the oxazolidinone

(20) X-ray data was deposited in the Cambridge Crystallographic Data Centre in CIF format as CCDC 269747 for 9.

nucleus (Scheme 4). The results support route I in the reaction mechanism (Scheme 2) because route II will retain the *S*-configuration to give *S*-oxazolidinone in the use of *S*-chloromethyloxirane. Accordingly, the synthesis of oxazolidinone is supposed to proceed via route I.

In conclusion, the present synthetic method is characterized by a simple procedure, mild reaction conditions, high reaction yield, and high selectivity and will be useful to produce various kinds of *N*-substituted-5-hydroxymethyloxazolidin-2-one and chiral oxazolidinone. The five-membered ring compound, oxazolidinone, is more stable than the six-membered ring compound, oxazinone.

### Experimental Section

**General Procedure for Oxazolidinone.** Primary amine (1 mmol ratio) was added to methanol (5 mL) containing an excess amount of halomethyloxirane (5 or 10 mmol ratio), K<sub>2</sub>CO<sub>3</sub> (5 or 10 mmol ratio), and TEA (5 or 10 mmol ratio) under reflux overnight. After the solution was cooled to room temperature, the reaction mixture was filtered for removing the solidified, unreacted carbonate salts. Then, the organic layer was evaporated and the residue was solved in AcOEt. The organic layer was washed with NaCl aq and dried using Na<sub>2</sub>SO<sub>4</sub>. The solvent was evaporated in vacuo. The residue was isolated by silica gel column chromatography with chloroform/methanol (10:1).

***N*-Benzyl-5-hydroxymethyloxazolidin-2-one (3b):** yield 88% as a pale yellow solid; mp 69–70 °C; IR (film) 3200–3620, 1730 cm<sup>-1</sup>; <sup>1</sup>H NMR (600 MHz, CDCl<sub>3</sub>) δ 3.32 (1H, dd, *J* = 6.5, 8.0 Hz), 3.44 (1H, dd, *J* = 8.0, 10.0 Hz), 3.62 (1H, dd, *J* = 13.0, 4.0 Hz), 3.85 (1H, dd, *J* = 13.0, 3.0 Hz), 4.38, 4.48 (d, 1H, *J* = 15.0 Hz), 4.58 (1H, m, *J* = 6.5, 10.0, 4.0, 3.0 Hz), 7.25–7.38 (5H, m); <sup>13</sup>C NMR (150 MHz, CDCl<sub>3</sub>) δ 45.1, 47.9, 62.6, 73.5, 127.7, 127.8, 128.6, 135.4, 156.2; MS (FAB) *m/z* 208 (*M* + H)<sup>+</sup>. Anal. Calcd for C<sub>11</sub>H<sub>13</sub>NO<sub>3</sub>: C, 63.76; H, 6.32; N, 6.76. Found: C, 63.59; H, 6.32; N, 7.01.

***N*-Benzyl-5-hydroxyoxazinan-2-one (4b).** To a methanol (4 mL) solution of bromomethyloxirane 2a (171 μL, 2.0 mmol) was added benzylamine (218 μL, 2.0 mmol). The reaction mixture was bubbled through CO<sub>2</sub> for 5 h and stirred overnight. The reaction mixture was evaporated in vacuo, and then the yellow residue was purified by silica gel column chromatography with chloroform/ethyl acetate (5:1) to give the pure product 4b (163 mg, 39% unoptimized yield) as a pale yellow solid: mp 114–115 °C; IR (KBr) 3200–3620, 1678 cm<sup>-1</sup>; <sup>1</sup>H NMR (600 MHz, CDCl<sub>3</sub>) δ 3.17 (1H, ddd, *J* = 12.0, 3.0 Hz), 3.38 (1H, dd, *J* = 12.0, 4.0 Hz), 4.10 (1H, m), 4.20 (1H, dd, *J* = 3.0, 12.0 Hz), 4.23 (1H, dd, *J* = 2.5, 12.0 Hz), 4.43, 4.61 (1H, d, *J* = 15.0 Hz), 7.24–7.32 (5H, m); <sup>13</sup>C NMR (150 MHz, CDCl<sub>3</sub>) δ 51.4, 52.7, 61.2, 70.5, 127.8, 128.1, 128.8, 136.2, 153.5; MS (ED) *m/z* 207 (*M*)<sup>+</sup>. Anal. Calcd for C<sub>11</sub>H<sub>13</sub>NO<sub>3</sub>: C, 63.76; H, 6.32; N, 6.76. Found: C, 63.62; H, 6.41; N, 6.66.

**(*R*)-*N*-(*p*-Bromobenzyl)-5-hydroxymethyloxazolidin-2-one (9).** *p*-Bromobenzylamine hydrochloride 1c (100 mg, 0.45 mmol) was removed by washing with NaOH aq; yield 82% as prisms; mp 109–110 °C (crystallized from ethyl acetate); [α]<sub>D</sub><sup>20</sup> = –12.5 (c 0.933, MeOH); IR (film) 3200–3620, 1729 cm<sup>-1</sup>; <sup>1</sup>H NMR (600 MHz, CDCl<sub>3</sub>) δ 3.32 (1H, dd, *J* = 7.0, 8.0 Hz), 3.40 (1H, dd, *J* = 8.0, 10.0 Hz), 3.57 (1H, dd, *J* = 12.0, 4.0 Hz), 3.83 (1H, dd, *J* = 12.0, 5.0 Hz), 4.32, 4.37 (1H, d, *J* = 15.0 Hz), 4.55 (1H, dt, *J* = 10.0, 7.0, 5.0, 4.0 Hz), 7.13, 7.45 (1H, d, *J* = 8.0 Hz); <sup>13</sup>C NMR (150 MHz, CDCl<sub>3</sub>) δ 45.0, 47.7, 62.9, 73.5, 121.9, 129.7, 131.9, 134.6, 157.9; MS (FAB) *m/z* 285, 287 (*M*)<sup>+</sup>. Anal. Calcd for C<sub>11</sub>H<sub>12</sub>NO<sub>3</sub>Br: C, 46.18; H, 4.23; N, 4.90. Found: C, 46.16; H, 4.28; N, 5.09.

**Supporting Information Available:** Experimental details. This material is available free of charge via the Internet at <http://pubs.acs.org>.

JO0501644

## HYDROLYSIS OF ANGIOTENSIN II RECEPTOR BLOCKER PRODRUG OLMESARTAN MEDOXOMIL BY HUMAN SERUM ALBUMIN AND IDENTIFICATION OF ITS CATALYTIC ACTIVE SITES

Shen-Feng Ma, Makoto Anraku, Yasunori Iwao, Keishi Yamasaki, Ulrich Kragh-Hansen, Noriyuki Yamaotsu, Shuichi Hirono, Toshihiko Ikeda, and Masaki Otagiri

Graduate School of Pharmaceutical Sciences, Kumamoto University, Kumamoto, Japan (S.-F.M., M.A., Y.I., M.O.); Department of Pharmacy, Miyazaki Medical College Hospital, Miyazaki, Japan (K.Y.); Department of Medical Biochemistry, University of Aarhus, Aarhus, Denmark (U.K.-H.); the School of Pharmaceutical Sciences, Kitasato University, Tokyo, Japan (N.Y., S.H.); and Drug Metabolism and Pharmacokinetics Research Laboratories, Sankyo Co., Ltd., Tokyo, Japan (T.I.)

Received June 21, 2005; accepted August 26, 2005

### ABSTRACT:

In the present study, we investigated the esterase-like activity of human serum albumin (HSA) and the mechanism by which it hydrolyzes, and thereby activates, olmesartan medoxomil (CS-866), a novel angiotensin II receptor antagonist. CS-866 has previously been shown to be rapidly hydrolyzed in serum in which HSA appeared to play the most important role in catalyzing the hydrolysis. We found that the hydrolysis of CS-866 by HSA followed Michaelis-Menten kinetics. Compared with the release of *p*-nitrophenol from *p*-nitrophenyl acetate (PNPA), CS-866 showed lower affinity to HSA and a lower catalytic rate of hydrolysis. Thermodynamic data indicated that PNPA has a smaller value of activation entropy ( $\Delta S$ ) than CS-866; consequently, PNPA is more reactive than CS-866. Ibuprofen and warfarin acted as competitive inhibitors of hydroly-

sis of CS-866, whereas dansyl-L-asparagine, *n*-butyl *p*-aminobenzoate, and diazepam did not. These findings suggest that the hydrolytic activity is associated to parts of site I and site II for ligand binding. All chemically modified HSA derivatives (Tyr-, Lys-, His-, and Trp-modifications) had significantly lower reactivity than native HSA; Lys-HSA and Trp-HSA had especially low reactivity. All the mutant HSAs tested (K199A, W214A, and Y411A) exhibited a significant decrease in reactivity, suggesting that Lys-199, Trp-214, and Tyr-411 play important roles in the hydrolysis. Results obtained using a computer docking model are in agreement with the experimental results, and strongly support the hypotheses that we derived from the experiments.

Ester prodrugs are hydrolyzed to their pharmacologically active metabolites after absorption. Esterases present in the small intestine, plasma, and liver are involved in this process. In most cases, intestinal esterases serve as the major enzymes in activation of prodrugs during the first pass through the gut after absorption. However, prodrugs that are relatively resistant to hydrolysis by intestinal esterases enter the blood circulation and are activated by serum (plasma) and liver esterases. The major hydrolyzing enzymes in serum are cholinesterase, arylesterase, carboxylesterase, and albumin. The relative importance of each serum esterase in prodrug activation varies among animal species and prodrugs.

Olmесartan medoxomil [CS-866: (5-methyl-2-oxo-1,3-dioxolen-4-yl) methoxy-4-(1-hydroxyl-1-methylethyl)-2-propyl-1-[4-[2-(tetra-

zol-5-yl)-phenyl]phenyl]methylimi-dazol-5-carboxylate] is a novel nonpeptide angiotensin II receptor antagonist that acts as an antihypertensive prodrug (Koike et al., 2001; Neutel, 2001; Brouil and Burke, 2003). After oral administration, CS-866 is rapidly de-esterified, producing an active acid metabolite, olmesartan (RNH-6270) (Fig. 1) (Koike et al., 2001; Neutel, 2001; Brouil and Burke, 2003). Hydrolysis of CS-866 in serum has been observed in several species, and comparison among five species has shown that hydrolytic activity is highest in rabbits, followed by dogs, mice, rats, and humans (Ikeda, 2000). Furthermore, it was found that differences in hydrolytic activity due to serum albumin are large compared to the combined activity of all serum components. Thus, HSA might make an important contribution to activation of CS-866 after oral administration.

In the present study, we examined the esterase-like activity of HSA and the mechanism of its hydrolysis of CS-866. First, the general properties of the hydrolytic reaction of HSA with CS-866 were determined, including the kinetics and thermodynamics, and compared with those of the hydrolytic reaction between HSA and *p*-nitrophenyl acetate (PNPA) (Means and Bender, 1975; Sakurai et al., 2004). Second, to characterize the effects of exogenous compounds on hydrolysis, we investigated changes in hydrolytic activity in the

This work was supported in part by a Grant-in-Aid for Scientific Research from the Ministry of Education, Science and Culture of Japan (11694298 for M.O.) and was also supported in part by Grant-in-Aid for Scientific Research, Encouragement of Young Scientists (B) (13771414 for N.Y.) from Japan Society for the Promotion of Science.

Article, publication date, and citation information can be found at <http://dmd.aspetjournals.org>.

doi:10.1124/dmd.105.006163.

**ABBREVIATIONS:** CS-866, olmesartan medoxomil [(5-methyl-2-oxo-1,3-dioxolen-4-yl) methoxy-4-(1-hydroxyl-1-methylethyl)-2-propyl-1-[4-[2-(tetrazol-5-yl)-phenyl]phenyl]methylimi-dazol-5-carboxylate]; RNH-6270, olmesartan; PNPA, *p*-nitrophenyl acetate; HSA, human serum albumin; rHSA, recombinant HSA; *n*-butyl *p*-AB, *n*-butyl-*p*-aminobenzoate; DNSA, dansyl-L-asparagine;  $\Delta G_T$ , free energy differences;  $\Delta G_S$ , free energy change for the initial reaction of albumin and substrate;  $\Delta G$ , activation free energy;  $\Delta H$ , activation enthalpy change;  $\Delta S$ , activation entropy change.